npj | parkinson's disease

Article

Published in partnership with the Parkinson's Foundation

https://doi.org/10.1038/s41531-025-01052-6

Parkinsonism disrupts cortical function by dysregulating oscillatory, network and synaptic activity of parvalbumin positive interneurons

Antea Minetti[1,8], Elena Montagni[1,2,8], Nicolò Meneghetti[3,4,8], Francesca Macchi[1], Éléa Coulomb[1,5], Alessandra Martello[1,6], Alexia Tiberi[1,5], Simona Capsoni[7], Alberto Mazzoni[3,4], Anna Letizia Allegra Mascaro[1,2] & Cristina Spalletti[1] ✉

Identifying novel and accessible therapeutic targets for Parkinson's Disease (PD) remains a pressing goal. Growing evidence implicates cortical dysfunctions in PD-related symptoms, yet the mechanisms —especially those involving parvalbumin-positive interneurons (PV-INs), key regulators of brain oscillations and plasticity—are not fully understood. In this study, we investigate how PD alters PV-IN network and cortical oscillatory dynamics using the 6-hydroxydopamine (6-OHDA) mouse model. Through an integrated approach combining electrophysiological recordings, wide-field calcium imaging, and histological analysis, we reveal a profound cascade of cortical changes. These include pathological hyperactivity above 100 Hz during movement and severe disruptions in PV-IN connectivity across the motor cortex. Synaptic imbalances and microglial activation further point to a multifaceted cortical response to dopaminergic degeneration, revealing inhibitory dysfunction, oscillatory instability, structural remodeling, and neuroinflammation. Our results link PD to cortical instability and highlight cortical plasticity as a promising target for therapeutic intervention.

Parkinson's disease (PD) is a chronic and progressive neurodegenerative disorder that primarily affects the motor system, impacting millions of individuals worldwide[1]. The hallmark of PD is the degeneration of dopaminergic neurons in the substantia nigra pars compacta (SNc) and the subsequent depletion of dopamine in the striatum. This dopamine deficiency disrupts the basal ganglia circuitry, leading to the characteristic motor symptoms of PD, including tremors, rigidity, bradykinesia, and postural instability[1–3].

Emerging evidence underscores the central role of dysfunctions within the basal ganglia-thalamo-cortical network in PD pathology. This network is critical for motor control, and its alterations profoundly affect the motor cortex, a region essential for voluntary movement and a promising target for therapeutic interventions[4–6]. A key feature of network dysfunctions is the disruption of cortical and subcortical oscillatory activity. Gamma-band oscillations, in particular, are crucial for motor planning and execution, as they facilitate neuronal synchronization and communication within the motor cortex[7]. Notably, PD patients exhibit a marked reduction in gamma-band oscillations within the basal ganglia-thalamo-cortical network, which correlates with motor dysfunction and symptom severity[8] and novel studies are evidencing the involvement of this circuit in PD pathophysiology[9].

The generation and maintenance of gamma-band oscillations depend heavily on GABAA receptor-mediated inhibition, primarily governed by parvalbumin-expressing interneurons (PV-INs)[10]. PV-INs are fast-spiking GABAergic cells that provide strong perisomatic inhibition to pyramidal neurons, regulating cortical network activity, excitatory-inhibitory (E/I) balance, and synchronized oscillatory rhythms[11–13]. Dopamine depletion has been shown to rapidly reduce PV expression in the striatum, suggesting early synaptic dysfunction in PV-INs[14]. In many cortical areas, thalamo-cortical afferents excite various types of inhibitory interneurons, but the

[1]Neuroscience Institute, National Research Council (CNR), 56124 Pisa, Italy. [2]European Laboratory for Non-Linear Spectroscopy (LENS), 50019 Sesto Fiorentino, Italy. [3]The Biorobotics Institute, Scuola Superiore Sant'Anna (SSSA), 56025 Pisa, Italy. [4]Department of Excellence for Robotics and AI, Scuola Superiore Sant'Anna (SSSA), 56025 Pisa, Italy. [5]Bio@SNS Laboratory of Biology, Scuola Normale Superiore (SNS), 56126 Pisa, Italy. [6]Interdisciplinary Health Science Center, Scuola Superiore Sant'Anna (SSSA), 56025 Pisa, Italy. [7]Section of Human Physiology, Department of Neuroscience and Rehabilitation, University of Ferrara, 44121 Ferrara, Italy. [8]These authors contributed equally: Antea Minetti, Elena Montagni, Nicolò Meneghetti. ✉e-mail: cristina.spalletti@in.cnr.it

strongest thalamic drive is directed toward PV-INs[15]. Recent studies in Parkinson's disease (PD) mice have shown that while thalamocortical recruitment of PV-INs remains intact, intracortical inhibitory synaptic transmission is altered. This finding raises new questions about the role of M1 inhibitory circuits during movement in the Parkinsonian state[16]. Despite growing evidence linking PV-IN dysfunction to basal ganglia pathology, the impact of dopamine depletion on cortical PV-INs and the mechanisms underlying cortical network remodeling in PD remains poorly understood.

Here, we provide a comprehensive functional and anatomical characterization of cortical dysfunctions in a 6-hydroxydopamine (6-OHDA) mouse model of PD. By combining longitudinal electrophysiological recordings, wide-field calcium imaging, and histological analyses, we investigate how dopaminergic degeneration affects PV-IN network connectivity, excitatory/inhibitory balance, and neuroinflammatory responses.

We revealed heightened coherence in the delta band in the striatum over time and increased above 100 Hz modulation in the motor cortex during voluntary movements.

This progressive breakdown of cortical network integrity is paralleled by disruptions in the cortical PV-IN network, particularly at later stages of pathological progression. These alterations were associated with synaptic remodeling, excitatory/inhibitory imbalance of cortical vesicular markers and heightened microglial phagocytic activity in the motor cortex.

These findings redefine PD as a network disorder and highlight the potential for cortical plasticity modulation as a therapeutic strategy. Understanding these mechanisms may open new avenues for developing interventions aimed at restoring cortical homeostasis and mitigating disease progression.

Results

Disrupted cortical and striatal circuit in the 6-OHDA mice

To induce a slow and stable loss of dopaminergic neurons and model Parkinson's Disease (PD), we unilaterally injected 6-hydroxydopamine (6-OHDA) into the striatum of adult mice, while control mice (CNT) underwent sham surgery with vehicle injection. For histological evaluation after 28 days post-lesion (DPL), tyrosine hydroxylase-positive (TH^+) immunohistochemistry in substantia nigra pars compacta (SNc) and in the caudate-putamen (CPu) was performed. In line with previous evidence[17], a pronounced loss of TH^+ neurons was observed in SNc of the injured hemisphere (Supplementary Fig. 1A, B; two-way ANOVA with Sidak's multiple comparisons test $F_{Groups \times Hemisphere}$ (1, 38) = 12.33 $p = 0.0012$, F_{Groups} (1, 38) = 30.61 $p < 0.0001$, $F_{Hemisphere}$ (1, 38) = 19.24 $p < 0.0001$; contra vs. ipsi 6-OHDA $p < 0.0001$; 6-OHDA vs. CNT ipsi $p < 0.0001$), along with a marked reduction in TH^+ fibers in CPu (Supplementary Fig. 1C, D; two-way ANOVA with Sidak's multiple comparisons test $F_{Groups \times Hemisphere}$ (1, 38) = 92.40 $p < 0.0001$, F_{Groups} (1, 38) = 53.77 $p < 0.0001$, $F_{Hemisphere}$ (1, 38) = 104.0 $p < 0.0001$; contra vs. ipsi 6-OHDA $p < 0.0001$; 6-OHDA vs. CNT ipsi $p < 0.0001$). We then longitudinally evaluated motor deficits by using the Cylinder Test. Our results confirmed a pronounced asymmetry in forelimbs use in 6-OHDA-lesioned mice, characterized by a reduced use of the paw contralateral to the injection without any recovery over time (Supplementary Fig. 1E, F; repeated two-way ANOVA with Sidak's multiple comparisons test $F_{Time \times Groups}$ (4, 76) = 16.88 $p < 0.0001$, F_{Time} (4, 76) = 16.54 $p < 0.0001$, F_{Groups} (1, 19) = 47.46 $p < 0.0001$, $F_{Subjects}$ (19, 76) = 5.143 $p < 0.0001$; 7DPL CNT vs. 6-OHDA $p < 0.0006$, 14DPL CNT vs. 6-OHDA $p < 0.0001$; 21DPL CNT vs. 6-OHDA $p < 0.0001$; 28DPL CNT vs. 6-OHDA $p < 0.0001$; one sample t-test with Holm-Sidak's multiple comparisons 6-OHDA Baselinse VS 7DPL $^{###}p = 0.0004$; 6-OHDA Baseline VS 14DPL $^{###}p = 0.0004$; 6-OHDA Baseline VS 21DPL $^{###}p = 0.0004$; 6-OHDA 28DPL $^{###}p = 0.0004$). The dopaminergic lesion affected both the substantia nigra and the striatum already by 7 DPL (Supplementary Fig. 1G, H; two-way ANOVA with Sidak's multiple comparisons test $F_{Groups \times Hemisphere}$ (1, 4) = 8.59 $p = 0.043$, $F_{Hemisphere}$ (1, 4) = 6.45 $p = 0.045$; contra vs. ipsi 6-OHDA $p = 0.035$; 6-OHDA vs. CNT ipsi $p = 0.041$, and Supplementary Fig. 1I; two-way ANOVA with Sidak's multiple comparisons test $F_{Groups \times Hemisphere}$ (1, 4) = 27.17 $p = 0.0065$, F_{Groups} (1, 4) = 9.05 $p = 0.040$, $F_{Hemisphere}$ (1, 4) = 50.72 $p = 0.0021$; contra vs. ipsi 6-OHDA $p = 0.0019$; 6-OHDA vs. CNT ipsi $p = 0.0087$). At this time point, we observed approximately a 47% reduction in dopaminergic cell bodies and a 50% loss of dopaminergic fibers in the striatum compared to the control group. By 28 DPL, the extent of the lesion remained relatively stable, with around 43% of dopaminergic cell bodies and 44% of dopaminergic fibers lost.

To evaluate how dopaminergic loss alters local oscillatory activity and coherence between the striatum and motor cortex, a chronic implant was placed for simultaneous electrophysiological recordings from both regions following 6-OHDA stereotaxic injection. Local field potentials (LFPs) were recorded weekly from awake, head-restrained mice in resting-state condition (Fig. 1A), when no forelimb movement was detected by the load cell.

The LFP of both groups displayed prominent delta oscillations, with a characteristic peak around 4 Hz, in both the striatum (Fig. 1B) and motor cortex (Supplementary Fig. 2A). In the striatum, the power of delta oscillations was modulated by both the recording stage and the experimental group. Over time, 6-OHDA mice demonstrated a clear trend of increasing delta power (Fig. 1C, two-way ANOVA $F_{Stages \times Groups} = 2.46$ $p = 0.08$, $F_{Stages} = 10.2$ $p = 0.0001$, $F_{Groups} = 8.51$ $p = 0.004$; 6-OHDA vs. CNT late stage $p = 0.0001$ Wilcoxon rank-sum test with Holm–Bonferroni correction). By the final recording stage, delta power in 6-OHDA mice was significantly higher compared to controls. This progressive increase suggests a temporal evolution of striatal oscillatory activity in 6-OHDA mice.

In the motor cortex, delta oscillations in 6-OHDA mice followed a similar upward trend across recording stages (Supplementary Fig. 2A). However, unlike in the striatum, this increase did not reach statistical significance when compared to the corresponding oscillations in controls (Supplementary Fig. 2B, two-way ANOVA $F_{Stages \times Groups} = 0.28$ $p = 0.75$, $F_{Stages} = 0.83$ $p = 0.44$, $F_{Groups} = 7.22$ $p = 0.008$).

Across both the striatum and motor cortex, power in other frequency bands, including beta, gamma and high-gamma, did not exhibit clear temporal trends or significant differences between the two groups (Supplementary Fig. 2B–H).

To confirm that this increase in delta power reflected genuine oscillatory activity and not shifts in the aperiodic (1/f-like) background, we used the FOOOF algorithm[18] to isolate and remove the aperiodic component of the striatal LFP power spectrum (see Materials and methods). After normalization, delta power in 6-OHDA mice progressively increased across sessions and became significantly higher than in controls at later stages in striatum (Supplementary Fig. 2I, J; two-way ANOVA; $F_{Stages \times Groups} = 6.28$, $p = 0.002$; $F_{Stages} = 25.6$, $p < 0.0001$; $F_{Groups} = 35.5$, $p < 0.0001$), replicating our original findings on the uncorrected PSD. Moreover, neither the aperiodic slope nor the offset of the power spectrum differed significantly between groups or across sessions in the striatum (Supplementary Fig. 2K; slope: two-way ANOVA $F_{Stages \times Groups} = 0.68$ $p = 0.7$, $F_{Stages} = 0.34$ $p = 0.72$, $F_{Groups} = 0.87$ $p = 0.35$ and Supplementary Fig. 2L; offset: two-way ANOVA $F_{Stages \times Groups} = 0.86$ $p = 0.4$, $F_{Stages} = 0.08$ $p = 0.92$, $F_{Groups} = 0.01$ $p = 0.94$), indicating that delta-band enhancements were not attributable to global spectral shifts. Consistent with this, FOOOF-corrected cortical PSDs showed that delta-band power followed a similar trajectory in both groups in the motor cortex, without significant differences between them (Supplementary Fig. 2M–P).

Next, we examined the relationship between the spectral features of LFPs in the striatum and motor cortex across the two experimental groups (Fig. 1D). To evaluate spectral connectivity between these regions, we computed spectral coherence (see Materials and methods). Both groups exhibited significant delta-band coherence between the striatum and motor cortex during the resting state (Fig. 1E), with coherence being significantly influenced by the recording stage. In the 6-OHDA group, delta coherence progressively and consistently increased over recording stages (Fig. 1E, two-way ANOVA $F_{Stages \times Groups} = 2.01$ $p = 0.13$, $F_{Stages} = 3.82$ $p = 0.02$, $F_{Groups} = 2.32$ $p = 0.10$; 6-OHDA vs. CNT late stage $p = 0.02$ Wilcoxon rank-

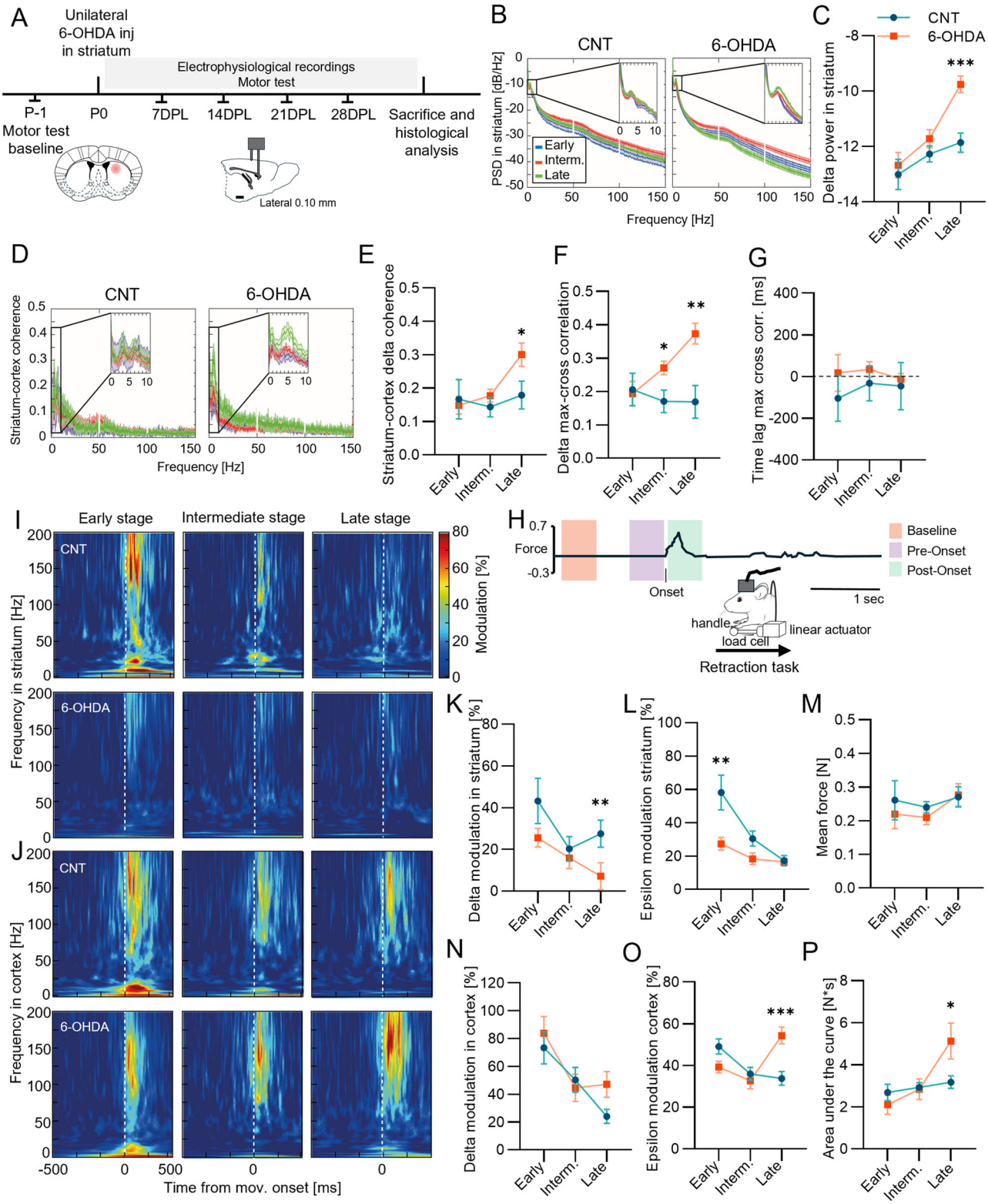

sum test with Holm–Bonferroni correction), culminating in a statistically significant difference from controls during the later recording stages.

To further explore this enhanced coupling, we computed the cross-correlation between the temporal dynamics of striatal and cortical delta power (Fig. 1F, two-way ANOVA $F_{Stages \times Groups} = 3.88$ $p = 0.02$, $F_{Stages} = 1.9$ $p = 0.15$, $F_{Groups} = 11.11$ $p = 0.001$; 6-OHDA vs. CNT intermediate stage $p = 0.004$, 6-OHDA vs. CNT late stage $p = 0.02$ Wilcoxon rank-sum test with Holm–Bonferroni correction). Consistent with the coherence findings, cross-correlation peaks demonstrated significant modulation across experimental groups and a significant interaction effect between group and recording week. In 6-OHDA-treated mice, cross-correlation of delta power between the striatum and motor cortex progressively increased over time, becoming significantly elevated compared to control mice as early as the intermediate stage post-toxin injection. These findings indicate that the neurodegenerative processes induced by 6-OHDA injection enhance delta-band coherence between the striatum and motor cortex.

Fig. 1 | Striatal delta activity and cortico-striatal coherence increase at rest in 6-OHDA mice. **A** Experimental protocol: (orange, $n = 13$) 6-OHDA (blue, $n = 8$ controls, CNT). Striatal and cortical LFPs simultaneously recorded weekly, during rest and motor task. Recording grouped into: early (week = 1); intermediate (weeks 2–3); late (week = 4). **B** Average power spectral density (PSD) of striatal LFPs in control and 6-OHDA mice across stages. Zoomed inset shows low-frequencies. **C** Delta power in striatal LFPs across weeks in CNT and 6-OHDA. **D** Striatal-cortical spectral coherence in CNT and 6- across stages. Zoomed inset: low-frequencies part of the PSD. **E** Delta-range coherence in CNT and 6-OHDA across stages. **F** Maximal cross-correlation across recording stages of the dynamics of delta power in control and 6-OHDA. **G** Optimal time lag for cross-correlation across recording stages of the dynamics of delta power in CNT and 6-OHDA mice. **H** Windows of analysis during the task in relation to movement onset. Black line: representative force trace throughout the task; the onset of the movement is highlighted. The orange window = baseline period, without movement detection; pink = pre-onset (movement preparation) and green = post-onset (movement). Average modulation of striatal (**I**) and cortical (**J**) LFPs time-frequency scalogram centered around movement onsets (vertical dashed white line) normalized by a baseline ([−1500,−750] ms before movement onsets) across stages in CNT ($n = 6$) and 6-OHDA ($n = 7$). **K**, **L** Modulation of delta and epsilon power in striatal LFPs around movement onsets (0–250 ms) across recording stages in CNT and 6-OHDA. **M** Variation of mean force exerted detected from the robotic M-platform in CNT and 6-OHDA. **N**, **O** Cortical delta and epsilon power modulation in CNT and 6-OHDA mice. **P** Area under the force curve detected from the robotic M-platform in CNT and 6-OHDA. Data are expressed as mean ± Standard Error of Mean. $^{*}p \le 0.05$; $^{**}p < 0.01$; $^{***}p < 0.001$; $^{****}p < 0.0001$. CNT (blue), 6-OHDA (orange). See also Supplementary Figs. 1 and 2 and Supplementary Table 1.

Finally, we investigated the time lag at which the maximum cross-correlation occurred between striatal and cortical delta power. No significant differences in the optimal time lag were observed between groups or across recording weeks (Fig. 1G, two-way ANOVA $F_{Stages \times Groups} = 0.14$ $p = 0.87$, $F_{Stages} = 0.2$ $p = 0.82$, $F_{Groups} = 1.37$ $p = 0.24$). This suggests the absence of a direct causal relationship in the temporal evolution of delta power between the striatum and motor cortex.

Voluntary movement induced increased epsilon spectral modulation in 6-OHDA mice motor cortex

Next, to identify specific alterations in motor function-related activity in the striatum and motor cortex, we investigated the spectral modulation induced by voluntary movement in both control ($n = 6$) and 6-OHDA ($n = 7$) mice. To this end, LFPs were simultaneously recorded from the cortex and striatum as the mice performed a voluntary forelimb retraction task using the M-Platform, a custom-designed apparatus for functional evaluation and neurorehabilitation of forelimb movement in mice[19–21].

The LFP recordings were segmented into time windows spanning from [−1500 ms to +500 ms] relative to movement onset, which was identified using a custom detection algorithm (see Materials and methods). Time-frequency scalograms were computed for each segment and normalized to a baseline period, defined as the average scalogram from [−1500 ms to −750 ms], with no force peak detected (Fig. 1H) for striatum (Fig. 1I) and cortex (Fig. 1J).

In control mice, voluntary movement elicited robust spectral modulation in the striatum, spanning a broad frequency range during the early recording stage (Fig. 1I, top-left). However, this modulation diminished progressively over time, and by the late recording weeks, little to no movement-related spectral activity was observed (Fig. 1I, top-right). In contrast, 6-OHDA mice exhibited minimal movement-induced spectral modulation in the striatum already from the early recording stage, with the only exceptions of delta and epsilon (Fig. 1I, bottom row and Supplementary Fig. 3A). Accordingly, striatal delta power modulation exhibited a decreasing trend in both control and 6-OHDA mice (Fig. 1K, two-way ANOVA $F_{Stages \times Groups} = 0.74$ $p = 0.48$, $F_{Stages} = 4.29$ $p = 0.01$, $F_{Groups} = 6.14$ $p = 0.01$; 6-OHDA vs. CNT late stage $p = 0.0033$ Wilcoxon rank-sum test with Holm–Bonferroni correction), though the reduction was more pronounced in 6-OHDA mice. By the late recording stage, 6-OHDA mice showed a complete loss of delta modulation, which led to a statistically significant difference between the two groups during this phase. Similarly, striatal epsilon modulation declined progressively in control mice across recording weeks (Fig. 1L, two-way ANOVA $F_{Stages \times Groups} = 5.02$ $p = 0.007$, $F_{Stages} = 15.4$ $p < 0.0001$, $F_{Groups} = 12.31$ $p = 0.0005$; 6-OHDA vs. CNT early stage $p = 0.0042$ Wilcoxon rank-sum test with Holm–Bonferroni correction). Interestingly, this pattern was not observed in 6-OHDA mice, where epsilon modulation in the early stage of recording was comparable to the levels seen in control mice at the end of the recording period (Fig. 1L).

A similar progressive reduction in spectral modulation was observed in cortical LFPs of control mice (Fig. 1J, top row). During the initial weeks of recording, voluntary movements elicited increases in power across multiple frequency bands, particularly in the delta, beta, and epsilon ranges (Fig. 1J, top-left and Supplementary Fig. 3B). However, this movement-induced spectral modulation diminished steadily over the course of the recording weeks. In 6-OHDA mice, a similar pattern of movement-induced spectral modulation was observed during the early recording stage (Fig. 1J, bottom-left and Supplementary Fig. 3B), with increases in delta, beta, and epsilon power. Over time, however, spectral modulation in these mice decreased in a manner that paralleled the trend seen in controls, except in the epsilon range, where an opposing trajectory emerged. Specifically, delta power modulation in the cortex followed a similar declining trajectory in both control and 6-OHDA mice, with a gradual reduction over recording weeks (Fig. 1N, two-way ANOVA $F_{Stages \times Groups} = 0.76$ $p = 0.46$, $F_{Stages} = 8.54$ $p = 0.0002$, $F_{Groups} = 1.01$ $p = 0.31$). In contrast, epsilon power modulation displayed divergent trends between the two groups (Fig. 1O). Epsilon progressively decreased in control mice over the recording weeks, while it increased steadily in 6-OHDA mice. By the late stages of recording, this divergence resulted in a statistically significant difference in epsilon modulation between the two groups (Fig. 1O, two-way ANOVA $F_{Stages \times Groups} = 6.68$ $p = 0.001$, $F_{Stages} = 3.17$ $p = 0.04$, $F_{Groups} = 3.99$ $p = 0.04$; 6-OHDA vs. CNT late stage $p = 0.001$ Wilcoxon rank-sum test with Holm–Bonferroni correction).

Although significant changes in cortical epsilon power modulation were observed, these changes did not translate into alterations in mean force output across the recording stages (Fig. 1M, repeated two-way ANOVA). The mean force remained stable in both control and 6-OHDA-treated mice, with no significant differences between the groups. However, the area under the force curve (AUC) increased significantly in 6-OHDA-treated mice during the late stage (Fig. 1P, repeated two-way ANOVA with Sidak's multiple comparisons test $F_{Stages \times Groups}$ (2, 33) = 4.88 $p = 0.014$, F_{Stages} (2, 33) = 6.83 $p = 0.0033$; 6-OHDA vs. CNT late stage $p = 0.037$). This increase likely indicates a reduction in the precision of movement, resulting in a more dispersed force profile over time. While the mean force output remains unchanged, its distribution appears less focused, suggesting an alteration in movement control in 6-OHDA-treated mice.

Finally, to further investigate the potential implications of cortical epsilon modulation in 6-OHDA-treated mice, we assessed its correlation with behavioral and cellular markers (Supplementary Fig. 3C). A significant negative correlation was observed between cortical epsilon power and performance in the behavioral test at 28 days post-lesion (Supplementary Fig. 3D), indicating that increased cortical epsilon activity might be associated with motor performance deficits. Additionally, cortical epsilon power was inversely correlated with the number of TH^+ cells in SNc (Supplementary Fig. 3E), as well as the intensity of TH^+ fibers in striatum (Supplementary Fig. 3F), indicating a link between increased cortical epsilon activity and dopaminergic degeneration. Together, these correlations provide a link between cortical spectral changes, cellular degeneration, and motor impairments, highlighting the complex interplay between neurophysiological, behavioral, and cellular adaptations in the 6-OHDA Parkinsonian model.

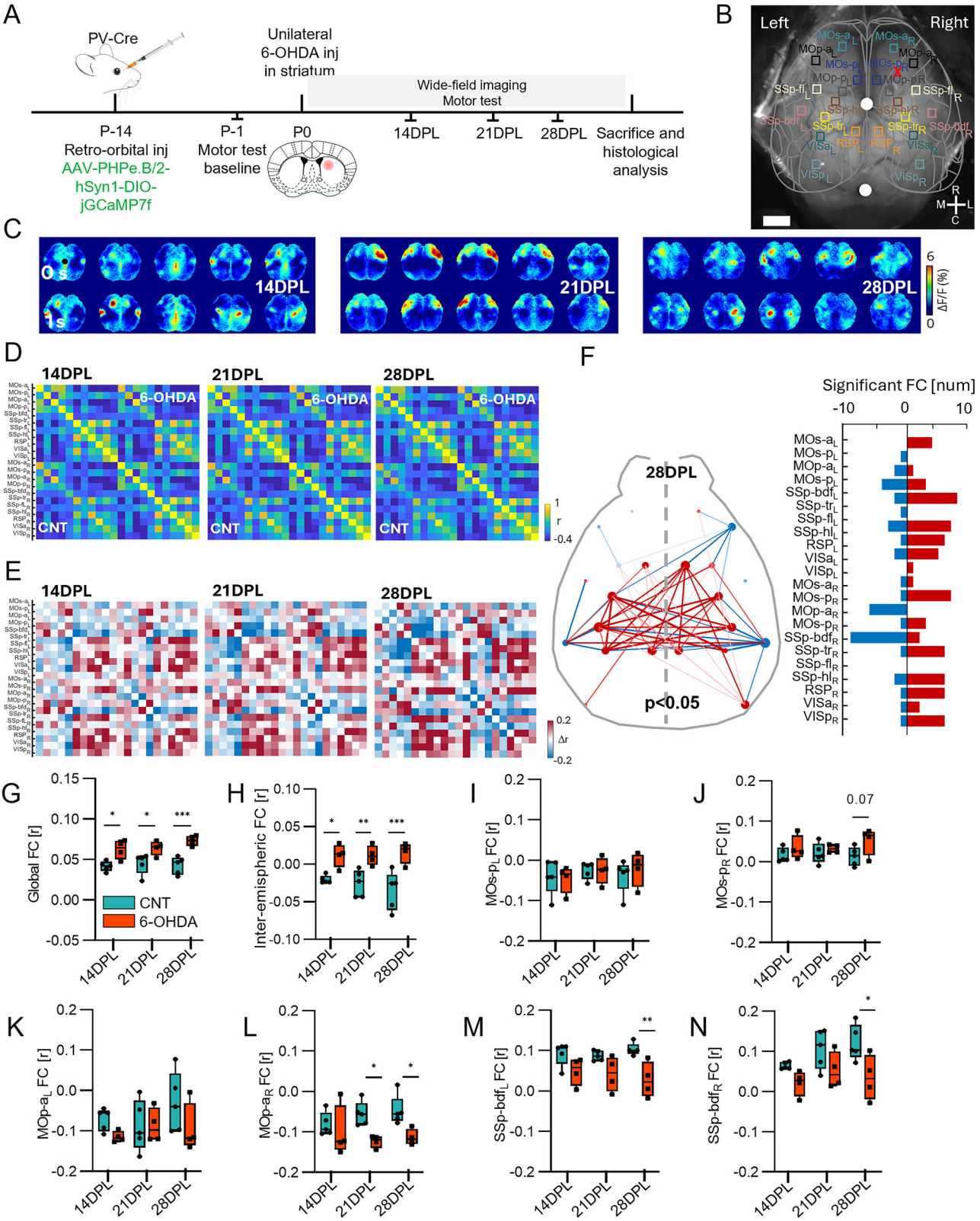

Dopaminergic neuron loss impact PV-INs functional cortical network

Electrophysiological results suggest that dopaminergic degeneration may affect broader cortical network connectivity. Specifically, increased epsilon modulation in the motor cortex of 6-OHDA mice pointed to a compensatory or maladaptive change in neuronal dynamics mediated by parvalbumin-positive interneurons (PV-INs)[11,22,23]. Therefore, we used wide-field (WF) calcium imaging to longitudinally investigate how functional cortical connectivity of PV-INs changed from 14 to 28 days post-lesion in 6-OHDA mice.

PV-Cre mice were administered retro-orbital injection with a PHP.eB serotype AAV expressing GCaMP7f under the parvalbumin (PV) promoter in a Cre-dependent manner. After 2 weeks, unilateral stereotaxic injection of 6-OHDA into the striatum was performed to generate the PD mouse model

Fig. 2 | Altered network of PV-INs rs-FC in 6-OHDA mice. A Experimental timeline for PV-INs longitudinal WF calcium imaging. **B** Representative WF field-of-view. Colored squares represent cortical ROI parcellation based on the Allen Brain Atlas. White dots indicate Bregma (top) and Lambda (bottom). Scale bar = 1 mm. **C** Representative 2-s sequences of resting state (RS) cortical activity at 14, 21 and 28 days post lesion (DPL) in control (CNT, top) and 6-OHDA group (bottom). Temporal sequences were randomly selected from the imaging dataset. **D** Dynamics of the average functional connectivity PV network (Pearson's correlation) over the days 14, 21, 28 DPL for CNT (bottom right) and 6-OHDA (top left). **E** FC differences matrix between CNT and 6-OHDA over the days, calculated by subtracting the average FC of the CNT group from that of the 6-OHDA group. Red = 6-OHDA hyperconnectivity; blue = 6-OHDA hypoconnectivity. **F** Network diagram of statistically significant FC alterations at 28 DPL (left). Red/blue lines represent significant hyper/ hypo-correlations of 6-OHDA compared with CNT, respectively. The bar plot (right) shows the number of significant FC (hypo left, hyper right) for each cortical area ($p < 0.05$, NBS). **G** Box plot showing the mean global signal PV-FC in the CNT group compared to the 6-OHDA group at 14,21 and 28 DPL.). **H** Box plot showing the mean inter-hemispheric PV-FC in the CNT group compared to the 6-OHDA group at 14, 21 and 28 DPL. PV-FC in the posterior area of the secondary motor cortex between CNT and 6-OHDA group at 14, 21 and 28 DPL in the left hemisphere (**I**) and right hemisphere (**J**). **C** Comparison of PV-FC in the anterior area of the primary motor cortex between CNT and 6-OHDA group at 14, 21 and 28 DPL in the left hemisphere (**K**) and right hemisphere (**L**). **M**, **N** Comparison of PV-FC in the barrelfield cortex between CNT and 6-OHDA group at 14, 21 and 28 DPL in the left hemisphere and right hemisphere. In blue, CNT $n = 5$ and in orange, 6-OHDA $n = 4$. Data are expressed as mean ± Standard Error of Mean. $^{*}p \leq 0.05$; $^{**}p < 0.01$; $^{***}p < 0.001$; $^{****}p < 0.0001$. See also Supplementary Fig. 3 and Supplementary Table 2.

(6-OHDA), with a control group receiving a vehicle injection (CNT). Then, weekly WF imaging and cylinder test were conducted starting from 14 days post lesion (DPL) for 3 weeks (Fig. 2A). The efficiency and specificity of viral infection were validated by post-mortem immunohistological inspection, showing that 90% of PV^{+} neurons were successfully transfected with the GCaMP, and 78% of $GCaMP^{+}$ neurons were effectively identified as PV^{+} neurons (Supplementary Fig. 4A, B). These findings confirm that PHP.eB transfection achieved both high efficacy and target specificity. Moreover, motor deficits in the use of the contralateral forelimb (Supplementary Fig. 4C, repeated two-way ANOVA with Sidak's multiple comparisons test $F_{\text{Time} \times \text{Groups}}$ (4, 45) = 11.8 $p < 0.0001$, F_{Time} (4, 45) = 11.5 $p < 0.0001$, F_{Groups} (1, 45) = 186.8 $p < 0.0001$; 14DPL CNT vs. 6-OHDA $p < 0.0001$; 21DPL CNT vs. 6-OHDA $p < 0.0001$; 28DPL CNT vs. 6-OHDA $p < 0.0001$; one sample *t*-test with Sidak's multiple comparisons test 6-OHDA Baseline VS 14DPL $^{\#\#\#}p = 0.0015$; 6-OHDA Baseline VS 21DPL $^{\#\#\#}p = 0.0016$, 6-OHDA Baseline VS 28DPL $^{\#\#\#}p = 0.0008$.), dopaminergic neuron loss in SNc (Supplementary Fig. 4D, two-way ANOVA with Sidak's multiple comparisons test $F_{\text{Groups} \times \text{Hemisphere}}$ (1, 18) = 13.40 $p = 0.0018$, F_{Groups} (1, 18) = 10.78 $p = 0.0041$, $F_{\text{Hemisphere}}$ (1, 18) = 7.595 $p = 0.013$; contra vs. ipsi 6-OHDA $p = 0.0008$; 6-OHDA vs. CNT ipsi $p = 0.0002$) and dopaminergic fibers in CPu (Supplementary Fig. 4E, two-way ANOVA with Sidak's multiple comparisons test $F_{\text{Groups} \times \text{Hemisphere}}$ (1, 18) = 21.61 $p = 0.0002$, F_{Groups} (1, 18) = 5.277 $p = 0.0338$, $F_{\text{Hemisphere}}$ (1, 18) = 35.19 $p < 0.0001$; contra vs. ipsi 6-OHDA $p < 0.0001$; 6-OHDA vs. CNT ipsi $p = 0.0002$) were validated, exhibiting a similar trend to that observed in the electrophysiological group.

In vivo imaging sessions were performed in awake, head-fixed mice at 14, 21 and 28 DPL for both CNT ($n = 6$) and 6-OHDA ($n = 5$) groups. Hemoglobin signal was removed from the calcium data, and global signal regression was applied to eliminate global signal contributions. Resting-state functional connectivity (rs-FC) was longitudinally assessed by defining a set of 22 regions of interest (ROIs) covering both the hemispheres (Fig. 2B, C). Correlation matrices were computed for each group using pairwise Pearson correlation (Fig. 2D). Differences in rs-FC between CNT and 6-OHDA groups were then quantified by comparing the average correlation matrices of injured mice to those of healthy controls at each time point (Fig. 2E). Results revealed abnormalities in the PV-INs cortical functional network, showing both hypo- and hyper-connectivity patterns in 6-OHDA mice, which appeared to gradually intensify over time (Fig. 2E). Using the network-based statistics (NBS), we therefore tested for significant changes in FC. Relative to the control group, 6-OHDA mice exhibited pronounced hyper-connectivity of the somatosensory areas. Decreased connectivity was instead observed bilaterally in the barrelfield cortex and predominantly in the primary motor cortex of the ipsilateral hemisphere to the lesion (Fig. 2F). Our results showed the emergence of a significantly altered network at 28 DPL, characterized by concurrent patterns of hypo- and hyper-connectivity across brain regions.

To identify the features contributing most to the network alterations, we studied FC dynamics globally and then we further categorized FC into inter-hemispheric or intra-hemispheric connections (Supplementary Fig. 4F). The 6-OHDA group consistently exhibited higher global FC values compared to the control group across all time points (Fig. 2G, Repeated two-way ANOVA with Sidak's multiple comparisons test F_{Groups} (1, 7) = 19.12 $p = 0.003$; 6-OHDA vs. CNT 14DPL $p = 0.014$; 21DPL $p = 0.024$; 28DPL $p = 0.0004$), suggesting a possible hypersynchronization of the circuitry. These differences increased over time, despite the control group remaining stable throughout, by reflecting an early and acute response to dopaminergic neuron loss. Interestingly, intra-hemispheric connectivity, both contralateral and ipsilateral to the lesion did not show any significant variation over time by highlighting that functional connections within a single hemisphere were more stable and less affected by the lesion (Supplementary Fig. 4G, repeated two-way ANOVA, and Supplementary Fig. 4H, repeated two-way ANOVA.). In contrast, transcallosal communications were significantly disrupted among cortical regions in 6-OHDA mice by contributing substantially to the network alterations over all time points investigated (Fig. 2H, repeated two-way ANOVA with 6-OHDA vs. CNT F_{Groups} (1, 7) = 19.49 $p = 0.0031$; 6-OHDA vs. CNT 14DPL $p = 0.0250$; 21DPL $p = 0.0094$; 28DPL $p = 0.0005$).

To further evaluate FC alterations potentially related to motor or sensory deficits, we then focused on three main regions of interest: the secondary and primary motor cortex, critical for movement regulation, and the barrelfield cortex, a key area for sensory processing in mice. The secondary motor cortex (MOs-p) showed stable FC over time in both contralateral- and ipsilateral hemispheres (Fig. 2I, J, repeated two-way ANOVA) by suggesting that this cortical region remains relatively resilient to dopaminergic neuron loss. A similar trend was observed also in the primary motor cortex of the contralateral hemisphere (Fig. 2K). In contrast, FC was significantly reduced as early as 21 DPL in the primary motor cortex of the ipsilateral hemisphere (Fig. 2L, repeated two-way ANOVA with Sidak's multiple comparisons test F_{Groups} (1, 7) = 13.66 $p = 0.007$; 6-OHDA vs. CNT 21DPL $p = 0.028$; 28DPL $p = 0.033$) indicating an early onset of alterations on motor regions. Barrel field cortex instead exhibited a trend toward hypoconnectivity in the 6-OHDA group with more pronounced effects in the contralateral hemisphere compared to the ipsilateral one (Fig. 2M, repeated two-way ANOVA with Sidak's multiple comparisons test F_{Groups} (1, 7) = 8.81 $p = 0.021$; 6-OHDA vs. CNT 21DPL $p = 0.028$; 28DPL $p = 0.0040$ and Fig. 2N, repeated two-way ANOVA with Sidak's multiple comparisons test F_{Time} (2, 14) = 4.71 $p = 0.027$, F_{Groups} (1, 7) = 7.15 $p = 0.032$; 6-OHDA vs. CNT 28DPL $p = 0.049$).

Taken together, these results suggest that while the pathological phenotype remains consistent over time, with an immediate and stable impairment, FC shows a progressive deterioration with the emergence of an altered network at 28 DPL. Notably, dopaminergic loss affects primarily inter-hemispheric connections by suggesting a stronger impact on the coordination between the two hemispheres.

Synaptic puncta output compensates for PV-INs deficiency in the hypoconnected areas

In the 6-OHDA mouse model, motor and sensory cortical areas exhibit disrupted functional connectivity of PV-IN networks. PV-INs play a critical role in synchronizing activity across cortical regions and generating gamma oscillations, which are essential for proper cortical processing. This dysfunction may underlie motor and cognitive deficits associated with Parkinson's disease[24].

Given their role in cortical synchrony and interhemispheric coordination, we investigated potential alterations in PV-IN density and synaptic connectivity. By analyzing PV^+ neurons and the surrounding puncta rings on non-PV neuronal somata in superficial layers II/III, we identified changes in the inhibitory network associated with dopaminergic loss.

PV^+ cell density was analyzed by assigning immunolabeled PV-INs to anatomically defined cortical layers, using Hoechst nuclear staining landmarks to delineate layers II/III in M2, M1, and S1BF (Fig. 3A). The layer-specific quantification revealed a significant reduction in PV-IN density in the 6-OHDA group compared to controls across all examined regions, including M2 (Fig. 3B, two-way ANOVA F_{Groups} (1, 14) = 39.66 $p < 0.0001$); 6-OHDA vs. CNT contra $p = 0.0009$, 6-OHDA vs. CNT ipsi $p = 0.0013$), M1 (Fig. 3C, two-way ANOVA F_{Groups} (1, 14) = 30.33 $p < 0.0001$; 6-OHDA vs. CNT contra $p = 0.0028$, 6-OHDA vs. CNT ipsi $p = 0.0038$), and S1BF (Fig. 3D, two-way ANOVA F_{Groups} (1, 14) = 8.607 $p = 0.0099$). The quantification of NeuN-positive cell density revealed no significant differences between the experimental groups, indicating that there is no general cortical cell loss (Supplementary Fig. 5A–C, two-way ANOVA). Therefore, the observed reduction in PV-IN signal likely reflects a downregulation of parvalbumin protein expression rather than a loss of PV-expressing interneurons in layer II/III.

The reduction in PV-IN density exhibited a symmetric distribution between hemispheres and consistent uniformity across cortical layers. Interestingly, quantitative analysis of presynaptic puncta-rings encircling non-PV neurons (Fig. 3E) revealed significant differences between experimental groups. Across all the three cortical areas investigated, a marked reduction in punta-ring intensity around non-PV neuronal somata was observed in the contralateral hemispheres of 6-OHDA mice (Fig. 3F–H). Conversely, the ipsilateral hemisphere of 6-OHDA mice showed no significant differences compared to the control and, in M1, presynaptic punta-ring density even appeared to be higher (Fig. 3F, two-way ANOVA with Sidak's multiple comparisons test $F_{Hemisphere}$ (1, 14) = 5.28 $p = 0.038$; contra vs. ipsi 6-OHDA $p = 0.036$; Fig. 3G two-way ANOVA with Sidak's multiple comparisons test $F_{Groups \times Hemisphere}$ (1, 14) = 14.80 $p = 0.0018$, $F_{Hemisphere}$ (1, 14) = 11.92 $p = 0.0039$; contra vs. ipsi 6-OHDA $p = 0.0005$; 6-OHDA vs. CNT contra $p = 0.011$; Fig. 3H, two-way ANOVA with Sidak's multiple comparisons test $F_{Groups \times Hemisphere}$ (1, 14) = 4.92 $p = 0.044$, F_{Groups} (1, 14) = 6.18 $p = 0.026$, $F_{Hemisphere}$ (1, 14) = 7.45 $p = 0.016$; contra vs. ipsi 6-OHDA $p = 0.010$. 6-OHDA vs. CNT contra $p = 0.010$).

These results revealed a discrepancy: despite the loss of PV-INs, inhibitory synaptic contacts did not appear to decrease proportionally. To further investigate this hypothesis, we analyzed the relationship between PV-IN reduction and puncta-ring density by normalizing PV puncta density to PV-IN density. In M2 (Fig. 3I, two-way ANOVA with Sidak's multiple comparisons test F_{Groups} (1, 14) = 12.79 $p = 0.0030$; 6-OHDA vs. CNT contra $p = 0.030$), there was a symmetric increase in the PV puncta density/PV-IN density ratio for 6-OHDA mice by suggesting a heavy compensatory mechanism in both the hemispheres. In M1 (Fig. 3J, two-way ANOVA with Sidak's multiple comparisons test $F_{Groups \times Hemisphere}$ (1, 14) = 7.93 $p = 0.014$, F_{Groups} (1, 14) = 17.58 $p = 0.0009$, $F_{Hemisphere}$ (1, 14) = 9.68 $p = 0.0077$; contra vs. ipsi 6-OHDA $p = 0.0028$; 6-OHDA vs. CNT contra $p = 0.0004$), the ipsilateral hemisphere of 6-OHDA mice exhibited the most significant increase in the ratio. In contrast, contralateral hemisphere values remained consistent with control levels, by suggesting a lack of compensatory upregulation. In S1BF of 6-OHDA mice (Fig. 3K, two-way ANOVA with Sidak's multiple comparisons test $F_{Groups \times Hemisphere}$ (1, 14) = 2.08 $p = 0.17$) instead there was a trend toward a higher ratio in the ipsilateral hemisphere. However, this compensation appears less pronounced compared to the motor regions.

Our results suggest that, despite the symmetric loss of PV-INs, their synaptic output is selectively upregulated in the ipsilateral hemisphere. This mismatch indicates the presence of a compensatory mechanism, potentially involving an increase in the strength of synaptic contacts formed by the long-range PV-INs to counterbalance the loss of inhibitory neurons.

To assess morphological complexity of PV-IN, we performed 3D dendritic reconstructions (Fig. 3L) and 3D Sholl analysis (Fig. 3M, two-way ANOVA with Sidak's multiple comparisons test F_{Radius} (139, 1820) = 199.2 $p < 0.0001$, F_{Group} (3, 1820) = 36.83 $p < 0.0001$), revealing a significant reduction in total branching points in the ipsilateral hemisphere of 6-OHDA-lesioned mice compared to the contralateral side (Fig. 3N, two-way ANOVA with Sidak's multiple comparisons test $F_{Groups \times Hemisphere}$ (1, 14) = 11.82 $p = 0.0040$, $F_{Hemisphere}$ (1, 14) = 11,45 $p = 0.0045$; contra vs. ipsi 6-OHDA = 0.0009; CNT vs. 6-OHDA ipsi $p = 0{,}032$). These findings suggest that dopamine depletion may induce dendritic atrophy in PV-INs, potentially disrupting local circuit organization, impairing their ability to maintain inhibitory network stability and recruiting long-range connections.

PV-INs functional connectivity predicts pathological progression

We then aimed to assess the potential of FC as a biomarker for disease progression in the 6-OHDA model of PD. To achieve this, we first integrated the entire dataset, encompassing both physiological and histological data, and performed principal component analysis (PCA) to determine whether the two groups could be distinctly separated. Indeed, PCA revealed clear clustering of control (CNT) and 6-OHDA groups along the first principal component (PC1), accounting for 46.5% of the variance (Fig. 4A). Among all features contributing to PC1, FC data ranked prominently, alongside puncta density and lesion assessments in the CPu, underscoring FC's relevance as a descriptor of disease progression (Fig. 4B). To further validate our findings, we trained a support vector machine (SVM) classifier using the entire dataset and various subsets. The classifier achieved an impressive 89% accuracy when trained with FC data from widefield recordings, while performance dropped to chance level (50%) in the shuffled (bootstrapped) condition, where data was randomly assigned to animals (Fig. 4C). We then examined patterns of correlations within the entire dataset using a correlation matrix (Fig. 4D). This analysis highlighted both positive and negative associations among the measured variables, with notable strong correlations observed between behavioral measures, FC parameters, and synaptic markers. Interestingly, much of the correlation between FC and other parameters was significant for FC data from the right hemisphere, corresponding to the injection site. An intriguing exception to this pattern was observed in the retrosplenial cortex, warranting further investigation (Fig. 4D). Examining specific correlations, we found that WF connectivity in cortical areas was strongly associated with the severity of motor deficits, underscoring its potential as a biomarker for disease progression. This relationship was particularly evident in cortical regions critical for motor processing, where alterations in PV-IN connectivity closely mirrored behavioral impairments (Fig. 4E). Moreover, PV-IN density exhibited a robust correlation with WF connectivity, suggesting that structural changes in inhibitory networks are intrinsically linked to functional connectivity deficits (Fig. 4F). Collectively, these findings indicate that while PV-IN density decreases across hypoconnected cortical regions in the 6-OHDA model, the concurrent reorganization of PV-IN synaptic connectivity—especially in the ipsilateral hemisphere—may represent a compensatory mechanism. This reorganization provides valuable insight into cortical dysfunction in PD models by highlighting the complex interplay between neuronal density and synaptic adaptations in preserving cortical network stability.

Excitatory/inhibitory imbalance and microglial response in the motor cortex following dopaminergic neurodegeneration

The striatum communicates indirectly with the motor cortex via basal ganglia circuitry while also receiving direct cortical modulation

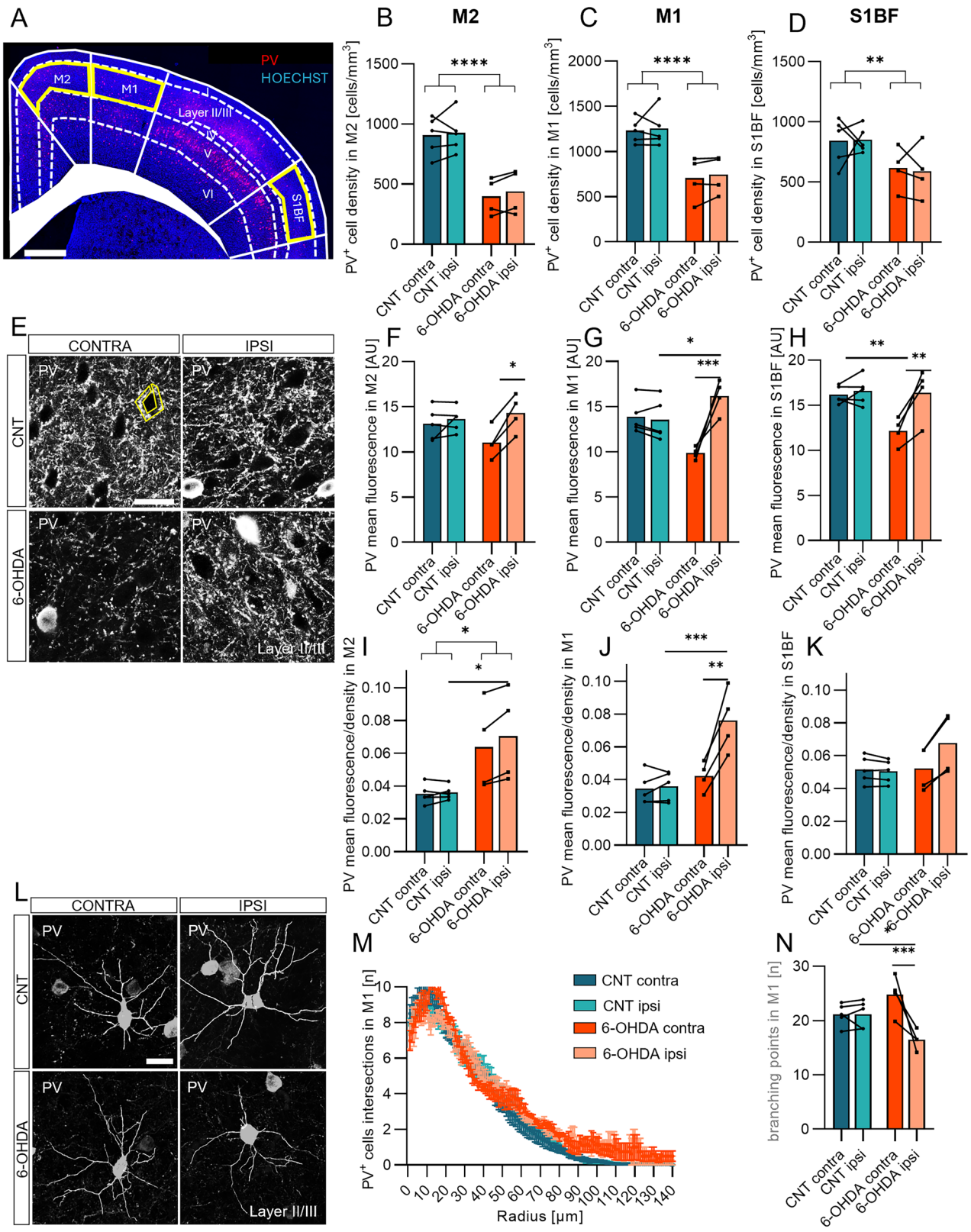

(Supplementary Fig. 5D). Given our observation of alterations in PV-IN connectivity—crucial for maintaining synchronized cortical activity—we investigated whether dopaminergic loss induces homeostatic changes in excitatory/inhibitory (E/I) balance or microglia (Supplementary Fig. 5E–G) within the motor cortex. To assess synaptic integrity, we analyzed cortical vesicular markers for both inhibitory (VGAT, Fig. 5A, B) and excitatory (VGLUT1, Fig. 5C, D; VGLUT2, Fig. 5E, F) neurotransmission. Specifically, we quantified the mean fluorescence of excitatory and inhibitory terminals impinging on the soma of layer II/III neurons and further examined synaptic integrity by evaluating vesicular markers as puncta-rings surrounding the cell body. Our findings revealed a pronounced E/I imbalance in the cortex of 6-OHDA-lesioned mice, characterized by significant

Fig. 3 | PV-INs density and PV puncta-rings and morphology in the cortex layer II/III. A Representative confocal image of a coronal brain section illustrating the distribution of PV^+ cells in the cerebral cortex of a PV-Cre mouse across the defined regions of interest, with a specific focus on layers II/III of M2, M1, and S1BF. Scale bar: 500 mm. Total PV+ cell density. **B** In M2. **C** In M1. **D** In S1BF. Unbiased stereology quantification of PV^+ cell density. **E** High magnification of the cortex immunostained with anti-PV for CNT and 6-OHDA groups. Interhemispheric analysis of anti-PV fluorescence mean values of puncta-rings, calculated in puncta-rings around cell bodies of non-PV positive neurons in control and 6-OHDA group. Scale bar, 20 µm. **F** In M2 interhemispheric analysis of anti-PV fluorescence mean values of puncta-rings in control and 6-OHDA group. **G** In M1. **H** In S1BF. **I–K** Normalized PV puncta density (PV puncta per PV-IN) in superficial layers of the ipsilateral and contralateral hemispheres across cortical regions in the controls and 6-OHDA group. **I** In M2. **J** In M1. **K** In S1BF. **L** IMARIS semi-automatic three-dimensional reconstruction and quantitative morphometric analysis of PV-IN. Scale bar, 20 µm. **M** Sholl analysis to study PV-IN morphology complexity in M1. **N** Interhemispheric analysis of PV-IN total branching points in control and 6-OHDA mice in M1. In blue, CNT $n = 5$ and in orange, 6-OHDA $n = 4$. Data are expressed as mean ± Standard Error of Mean. $^*p \le 0.05$; $^{**}p < 0.01$; $^{***}p < 0.001$; $^{****}p < 0.0001$. See also Supplementary Table 3.

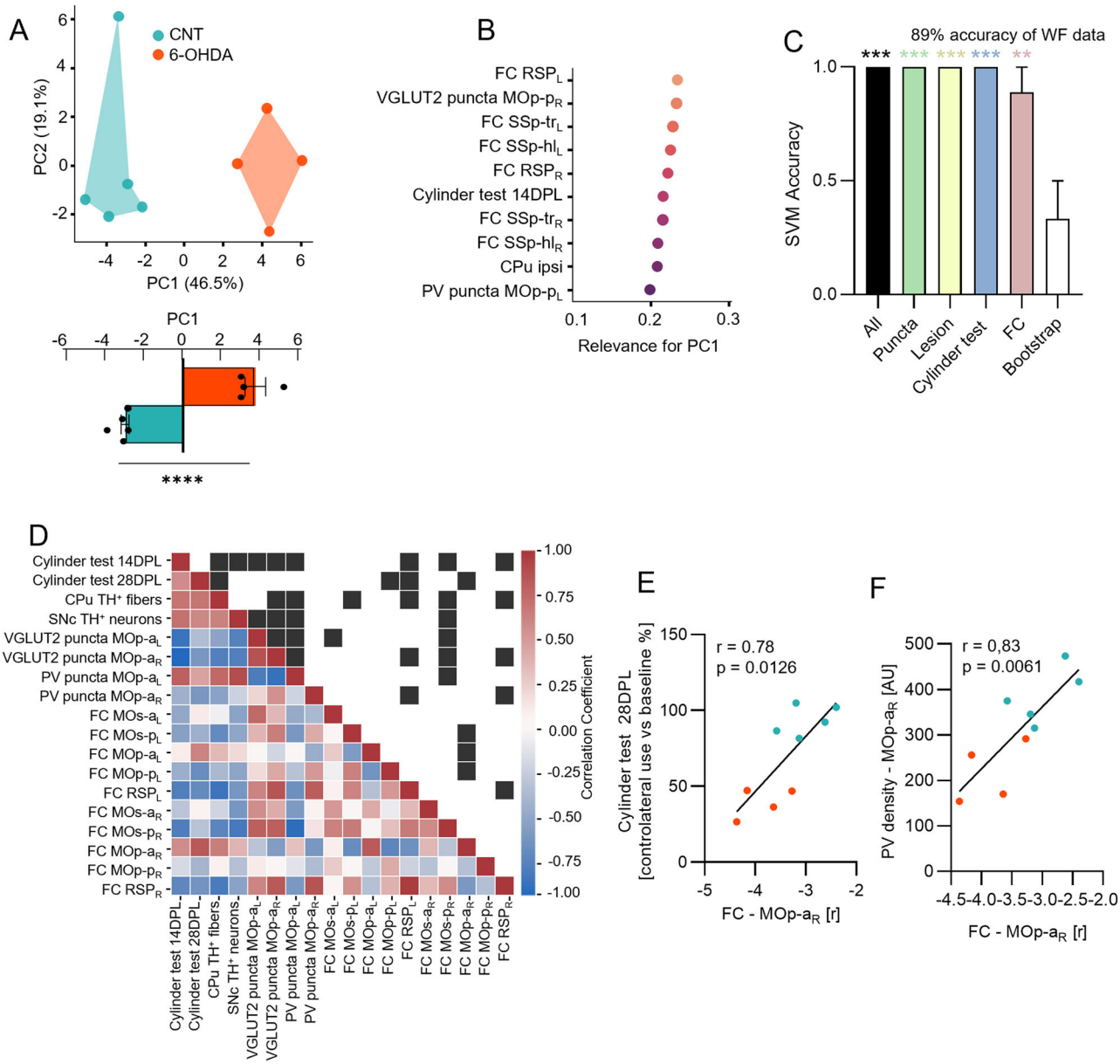

Fig. 4 | PV-INs functional connectivity predicts pathology progression. A Scatter plot on the principal component space showing the distribution of CNT and 6-OHDA mice on the first and second components. Unpaired *t*-test $p < 0.0001$. **B** First ten ranked features contributing to the PC1. **C** Average classification accuracy of the SVM classifier in distinguishing CNT and 6-OHDA mice using Leave-One-Out Cross-Validation (LOO-CV). The SVM was trained on different subsets of the dataset plus a bootstrap dataset as control, and accuracy was measured across all Leave-One-Out splits (Wilcoxon signed rank test (against chance: 0.5): All, $p = 0.0039$; Puncta, $p = 0.0039$; Lesion, $p = 0.0039$; Cylinder test, $p = 0.0039$; WF, $p = 0.0391$). **D** Heat map representing values from the correlation matrix (Pearson correlation) of analyzed parameters (bottom triangle), and the significance of each pairwise comparison (top triangle: black box indicates $p < 0.05$). **E, F** Scatter plot and linear regression detailing specific correlations depicted in (**D**). In particular, we show the correlation between wide-field data at 28DPL in the MOp-a$_R$ with **E** performance in the cylinder test at 28DPL, and **F** PV density in MOp-pR (*r* and *p* values are indicated in the figures). All the FC data refer to FC at 28DPL. In blue, CNT $n = 5$ and in orange, 6-OHDA $n = 4$. Data are expressed as mean ± Standard Error of Mean. $^*p \le 0.05$; $^{**}p < 0.01$; $^{***}p < 0.001$; $^{****}p < 0.0001$.

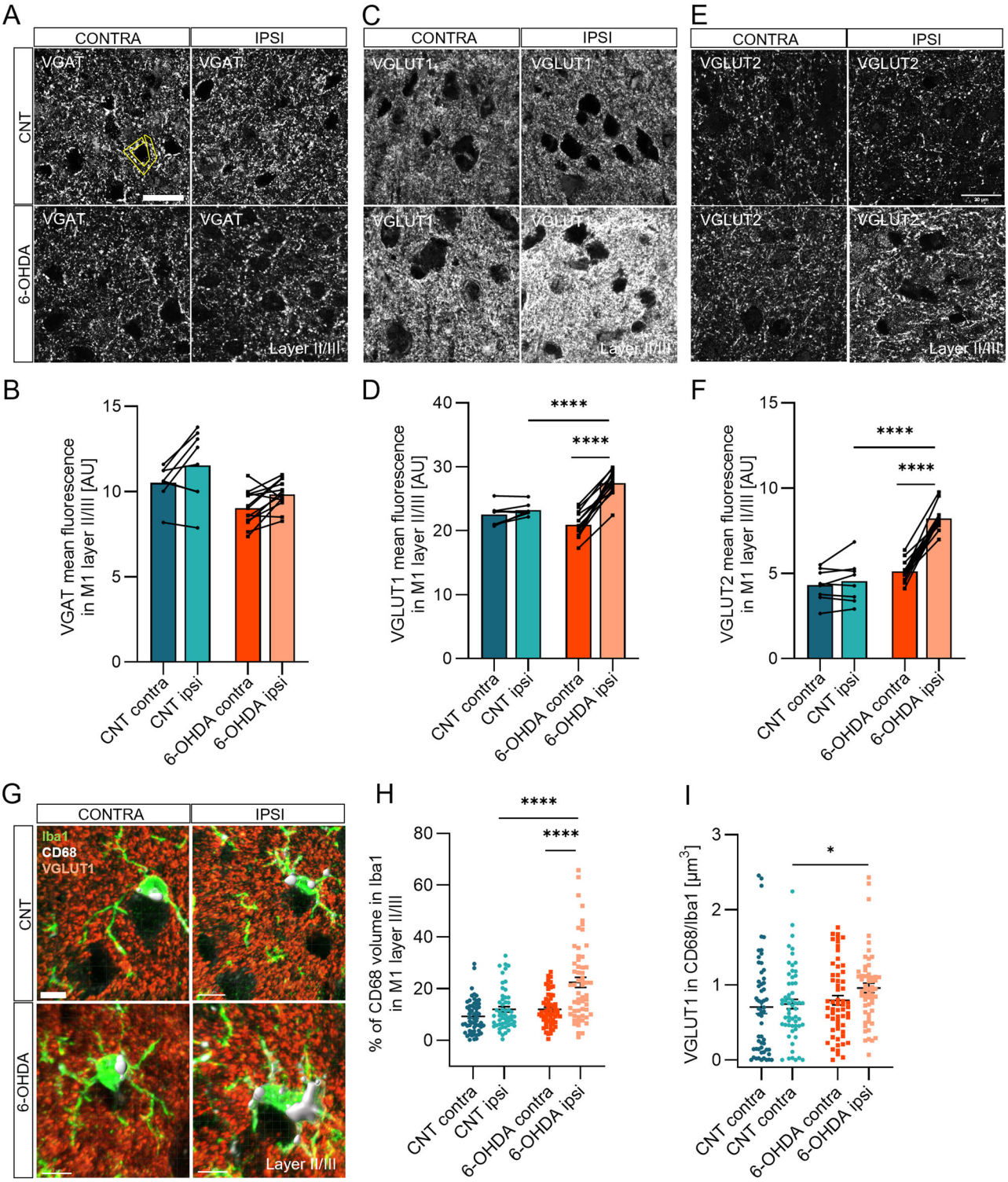

Fig. 5 | Modulation of excitatory and inhibitory transporters and microglia activation after 6-OHDA injection. A VGAT puncta-rings analysis. Magnified view of the primary motor cortex layer II/III stained with anti-VGAT for control. Scale bar: 20 µm. **B** Interhemispheric analysis of anti-VGAT fluorescence mean values of puncta-rings around cell bodies in control ($n = 8$) and 6-OHDA group ($n = 13$), calculated in perisomatic puncta-rings intensity around cell bodies. **C** VGLUT1 puncta-rings analysis in layer II/III of control and 6-OHDA groups. Magnified view of the primary motor cortex stained with anti-VGLUT1. Scale bar: 20 µm. **D** Interhemispheric analysis of anti-VGLUT1 fluorescence mean values of puncta-rings in control ($n = 8$) and 6-OHDA group ($n = 13$). **E** VGLUT2 puncta-rings analysis in layer II/III of control and 6-OHDA groups. Magnified view of the primary motor cortex stained with anti-VGLUT2. Scale bar: 20 µm. **F** Interhemispheric analysis of anti-VGLUT2 fluorescence mean values of puncta-rings in control ($n = 8$) and 6-OHDA group ($n = 13$). **G–I** Phagocytosis analysis of Iba1-positive cells in the primary motor cortex layer II/III. **G** Representative tridimensional surface analysis of Iba1, CD68 and VGLUT1 markers in the primary motor cortex stained with anti-Iba1, anti-CD68 and anti-VGLUT1. Scale bar: 7 µm. **H** Interhemispheric analysis of phagosome volume ($CD68^+$) inside $Iba1^+$ cells. $n = 60$ cells for each dataset and CNT animals $n = 4$ vs. 6-OHDA animals $n = 5$ were analyzed. **I** Interhemispheric analysis of VGLUT1 engulfment inside CD68 volume, normalized on the total amount of VGLUT1 in the field. $n = 60$ cells for each dataset and CNT animals $n = 4$ vs. 6-OHDA animals $n = 5$ were analyzed. Data are expressed as mean ± Standard Error of Mean. $^*p \leq 0.05$; $^{**}p < 0.01$; $^{***}p < 0.001$; $^{****}p < 0.0001$. See also Supplementary Fig. 5 and Supplementary Table 4.

alterations in the density of these synaptic markers, highlighting potential compensatory mechanisms in response to dopaminergic degeneration.

For VGAT, expression levels remained stable, with no significant changes observed, suggesting that inhibitory neurotransmission, represented by VGAT puncta-ring density, was unaffected by dopaminergic loss at the group level. Interhemispheric analysis of anti-VGAT fluorescence mean values confirmed this, showing no significant interaction between the animal groups and hemispheres (Fig. 5B, two-way ANOVA with Sidak's multiple comparisons test $F_{\text{Groups} \times \text{Hemisphere}}$ (1, 38) = 0.01178 $p = 0.9144$, F_{Groups} (1, 38) = 10.58 $p = 0.0024$, $F_{\text{Hemisphere}}$ (1, 38) = 3.048 $p = 0.0.0889$). In contrast, for VGLUT1, a significant increase was observed in the ipsilateral hemisphere, suggesting that excitatory synaptic transmission was globally enhanced following dopaminergic lesioning. The interhemispheric comparison further reinforced this trend, with pronounced differences observed in the ipsilateral hemisphere of the 6-OHDA group compared to controls (Fig. 5D, two-way ANOVA with Sidak's multiple comparisons test $F_{\text{Groups} \times \text{Hemisphere}}$ (1, 38) = 26.21 $p < 0.0001$, F_{Groups} (1, 38) = 5.374 $p = 0.026$, $F_{\text{Hemisphere}}$ (1, 38) = 40.01 $p < 0.0001$; ipsi 6-OHDA vs. CNT $p < 0.0001$; 6-OHDA vs. CNT ipsi $p < 0.0001$). Similarly, VGLUT2 expression was significantly upregulated in ipsilateral (Fig. 5F, two-way ANOVA with Sidak's multiple comparisons test $F_{\text{Groups} \times \text{Hemisphere}}$ (1, 38) = 27.21 $p < 0.0001$, F_{Groups} (1, 38) = 64.94 $p < 0.0001$, $F_{\text{Hemisphere}}$ (1, 38) = 36.56 $p < 0.0001$; contra vs. ipsi 6-OHDA $p < 0.0001$; 6-OHDA vs. CNT ipsi $p < 0.0001$), highlighting that the E/I imbalance in the 6-OHDA model is largely driven by elevated mean fluorescence of puncta-rings in the ipsilateral hemisphere. Emerging evidence underscores the central role of dysfunctions within the basal ganglia-thalamo-cortical network[25,26], focusing the analysis on the portion of VGLUT1 and VGLUT2 signal surrounding cell bodies of layer II/III, we revealed an increased expression in 6-OHDA-treated mice. Unlike traditional approaches that generalize synaptic marker quantification across the entire field of view-reporting values such as percentage of area, mean fluorescence intensity, or stereological density (Supplementary Fig. 6: PV A–C, VGAT D–F, VGLUT1 G–I, VGLUT2 J–L)—we opted for a more biologically meaningful method by specifically analyzing the perisomatic expression of synaptic puncta surrounding individual neuronal somata, recognizing that this reflects a specific subset of excitatory inputs, rather than the majority, which target dendrites. This approach enables precise assessment of axo-somatic connections, which play a crucial role in modulating neuronal output. In contrast, whole-field analyses include a broader range of synaptic contacts, including axo-dendritic and axo-axonic inputs. Therefore, the two methodologies offer complementary insights into synaptic architecture and plasticity. These findings suggest an adaptive response to the loss of dopaminergic input, characterized by a pronounced E/I imbalance, likely aimed at compensating for the reduced inhibitory influence in the lesioned cortex.

These findings suggest that the loss of dopaminergic input triggers an adaptive response in the motor cortex, characterized by a pronounced E/I imbalance, likely aimed at compensating for the reduced dopaminergic and altered PV-IN influence in the lesioned hemisphere. Given the crucial role of microglial in synaptic remodeling, we further examined their involvement in these cortical alterations. As the brain's resident phagocytes, microglia actively remove dead and dying neurons, as well as synapses[27]. In PD and related models like the 6-OHDA lesion, microglial activation often parallels dopaminergic neuron degeneration and is thought to exacerbate or even trigger pathological changes in the cortex[28,29]. Given microglia's pivotal role in synaptic remodeling especially during brain injury[30–32], we thus investigated their role in the observed synaptic modulation in 6-OHDA treated mice. First, we analyzed microglial density in cortical areas with identified connectivity deficits and observed no significant changes in the cortex (Supplementary Fig. 5E–G).

Then, we proceeded to quantify microglial phagocytic ability using CD68 as a marker (Fig. 5G). CD68 is a lysosomal and endosomal marker associated with phagocytosis, specifically expressed by macrophages, including Iba1-positive microglia in the CNS[33]. Interestingly, we found an increase in CD68 in microglia in the ipsilateral cortex of 6-OHDA treated mice, suggesting an enhanced microglia engagement in phagocytic activity (Fig. 5H, two-way ANOVA with Sidak's multiple comparisons test $F_{\text{Groups} \times \text{Hemisphere}}$ (1, 228) = 9.03 $p = 0.0030$, F_{Groups} (1, 228) = 25.85 $p < 0.0001$, $F_{\text{Hemisphere}}$ (1, 228) = 26.08 $p < 0.0001$; contra vs. ipsi 6-OHDA $p < 0.0001$; 6-OHDA vs. CNT ipsi $p < 0.0001$). Additionally, there was an increased engulfment of VGLUT1 by microglia (Fig. 5I, two-way ANOVA with Sidak's multiple comparisons test F_{Groups} (1, 228) = 5.00 $p = 0.026$; 6-OHDA vs. CNT ipsi $p = 0.053$). This suggests that microglia are actively participating in the removal of synaptic components, which may be a response to neuronal damage and synaptic remodeling associated with dopaminergic degeneration.

Discussion

Cortical network dynamics, together with the correct excitatory/inhibitory balance and immune response could be promising targets to slow down Parkinson's disease (PD) progression. This study provides compelling evidence that subcortical dopaminergic degeneration in a 6-OHDA PD model[1,34], significantly impacts not only cortico-striatal electrophysiological coupling but also functional and anatomical cortical features related to the inhibitory system, specifically Parvalbumin-positive interneurons (PV-INs). Through a combination of electrophysiological recordings, wide-field calcium imaging, and histological analyses, we uncovered a remodeling mechanism of cortical plasticity involving PV-INs in response to nigrostriatal degeneration.

The 6-OHDA PD mouse model is known to primarily induce localized dopaminergic depletion, yet it provides valuable insight into early-stage Parkinson's disease pathology. Although less commonly used for studying cortical alterations compared to the medial forebrain bundle (MFB) lesion model, cortical changes in this model may arise through several indirect mechanisms. These include disruption of basal ganglia–thalamocortical circuits, neuroinflammatory responses with potential long-range effects, compensatory cortical plasticity, and altered neuromodulatory tone in non-dopaminergic systems. These mechanisms likely contribute to the structural and physiological cortical changes observed in our study, despite limited direct cortical dopamine loss.

Electrophysiological analysis of both the striatum and motor cortex, focusing on their functional coupling in resting state, revealed a significant increase in striatal delta band activity in 6-OHDA mice, consistent with previous studies (Fig. 1C)[35,36]. Although direct changes in motor cortex activity at rest were not observed, we identified a progressive increase in cortico-striatal coherence in the delta band as the pathology advanced (Fig. 1F). Interestingly, the rise in striatal delta power alone does not fully account for the observed increased cortico-striatal coherence, as these phenomena can occur independently though related[37]. Indeed, elevated striatal delta power reflects increased local oscillatory activity, whereas increased coherence in the delta band may reflect a more consistent phase relationship, correlated spectral amplitude fluctuations, or shared inputs between the cortex and striatum[38,39]. This distinction suggests that the 6-OHDA-induced neurodegeneration drives pathological entrainment of cortico-striatal communication, potentially contributing to disrupted cortical network dynamics in Parkinson's disease.

Notably, we did not detect significant changes in beta-band activity between CNT and 6-OHDA mice. This is consistent with broader literature, which suggests that beta-band oscillations (13–30 Hz) are not as prominently elevated in mouse models of PD as in humans or other animal models such as rats and non-human primates. While beta activity is a hallmark of PD in patients, non-human primates, and rats, its expression in mice is more variable and generally less pronounced. For example, increases in beta power have been reported in cortical slices from 6-OHDA–treated mice[40] and in vivo during locomotion[40]. However, several studies have failed to observe such increases following 6-OHDA treatment[35,41], instead reporting enhanced low-frequency activity in the delta band, consistent with our findings.

This variability likely reflects species-specific differences in basal ganglia–thalamocortical circuitry, as well as the extent of dopaminergic

neuron loss typically achieved in mouse 6-OHDA models. In our study, we did not observe significant changes in beta-band power in the motor cortex of lesioned mice, aligning with prior reports that question the reliability of beta oscillations as a biomarker of network dysfunction in mouse PD models[35]. These observations highlight the need to interpret cross-species electrophysiological signatures with caution and suggest that alternative frequency bands, such as low-frequency below 5 Hz, may offer more informative readouts in mice.

During voluntary movement, we instead observed stark differences in spectral modulation between 6-OHDA-treated and control mice. In the striatum of 6-OHDA mice, spectral modulation was essentially absent from the earliest recording stages, indicating that the neurotoxin rapidly disrupts movement-related subcortical oscillatory activity (Fig. 1I). In contrast, control mice exhibited robust movement-related spectral modulation in the striatum during the voluntary retraction task, underscoring the early impact of 6-OHDA on striatal function (Fig. 1J).

Interestingly, in control mice, spectral modulation gradually decreased in both the striatum and cortex over the recording weeks (Fig. 1I, J). This progressive reduction in movement-related spectral modulation observed in control mice may reflect both task automatization and gradual signal degradation, two non-mutually exclusive phenomena. Reduced spectral power in motor cortex is consistent with event-related desynchronization during learned movements[42–45], and may indicate more efficient cortical recruitment as the task becomes familiar. Despite this overall trend, we observed an opposing pattern in the epsilon range in the motor cortex of 6-OHDA mice, where epsilon power progressively increased throughout recording weeks (Fig. 1O). This heightened epsilon-band modulation may reflect either network hypersynchrony or increased neuronal firing near the electrode tip, potentially driven by reduced inhibitory tone following PV-IN loss. Gamma oscillations have been reported to arise from balanced interactions between excitatory pyramidal neurons and inhibitory interneurons, particularly PV-positive cells, which generate synchronous activity in the 30–80 Hz range[46–49]. In contrast, epsilon-band activity (>100 Hz) is thought to reflect a different physiological mechanism, often linked to increased local population firing or asynchronous high-frequency events, rather than structured E-I coupling[50–52]. Disinhibition-driven hyperactivity of principal neurons could thus underlie the increased epsilon power observed here, despite PV-IN loss. Disentangling these mechanisms will require future studies incorporating spike-sorted unit recordings to track PV interneuron activity during 6-OHDA–induced nigrostriatal degeneration. These findings underscore the dual role of cortical and subcortical dynamics in PD pathology, where the motor cortex undergoes spectral changes to compensate for striatal dysfunction. Indeed, the parameters extracted by the M-Platform regarding the motor performance during the retraction task revealed that, despite a conserved mean force output across the recording stages (Fig. 1M), the area under the force curve (AUC) increased significantly in the late stage of the pathology (Fig. 1P). This parameter indicates a more dispersed force profile, which is a form of movement alteration but can be also considered a compensatory mechanism to accomplish the task. For the same reason epsilon power increase may represent either a maladaptive or a compensatory plastic arrangement. However, the progressive divergence in spectral patterns, particularly the rise in epsilon modulation during movement, highlights the probable maladaptive nature of these compensations.

Previous research showed that PV-INs are key regulators of cortical inhibition control and suggested that gamma oscillations regulated by PV-INs promote synaptic plasticity in cortical motor areas[7,12,23,53–55]. We therefore longitudinally investigated alterations in PV-INs cortical network using wide-field calcium imaging (Fig. 2). Electrophysiological and imaging analyses revealed that while the pathological phenotype remains stable over time (Supplementary Fig. 1F), FC undergoes progressive deterioration with the most pronounced alterations emerging at 28 days post-lesion (Fig. 2F). Critically, inter-hemispheric connectivity was strongly affected already at early time points (Fig. 2H), indicating that dopaminergic loss impacts cortical communication between hemispheres more than intra-hemispheric connections. Focusing on key regions, we found that the posterior secondary motor cortices (MOs-p) bilaterally, and the contralateral primary motor cortex, appear particularly resilient to dopaminergic damage (Fig. 2I–K). In contrast, the ipsilateral primary motor cortex remains a primary site affected by dopaminergic disruption (Fig. 2L). Notably, the Barrel Field (S1BF) cortex showed marked hypoconnectivity in the 6-OHDA group, especially contralaterally (Fig. 2M, N). Although not a direct target of dopaminergic degeneration, S1BF is functionally influenced by the nigrostriatal pathway and is vulnerable to dopamine loss[56], which may impair whisker-guided tactile processing and contribute to sensory non-motor symptoms[57]. These results suggest that S1BF plays a role in disrupted sensory integration and may underlie sensorimotor alterations in Parkinsonism. However, its role remains insufficiently understood and warrants further study to clarify the broader cortical impact of dopaminergic loss. Moreover, considering the established link between resting state FC (rs-FC) and the power coherence in low-frequency bands[58–60], the hypersynchronized Calcium dynamics observed could be possibly driven by the increased delta band synchronization.

Although our findings suggest a disruption of inter-hemispheric communication, further investigation into PV-IN density, morphology and synaptic connectivity (Fig. 3) provides critical insights into the role of the healthy hemisphere in the compensatory mechanisms that reshape PV-IN cortical network. Our findings indicate a decrease in the expression of Parvalbumin in the cell bodies of both ipsilesional and contralesional hemispheres which is an indirect signal of re-opening of cortical plasticity. PV-IN, together with other classes of inhibitory interneurons, are indeed considered plasticity 'brakes'[61] and their reduction has already been identified as a marker of motor improvement induced by rehabilitation[62] and of the reopening of cortical plasticity that is the basis for network reorganization and functional recovery[63]. This is in line with the functional reorganization of PV-IN connections across the two hemispheres evidenced by the wide-field experiment. Indeed, despite a symmetric reduction in PV-IN density across hemispheres and cortical layers (Fig. 3B–D), we observed a selective upregulation of inhibitory synaptic output in the ipsilateral hemisphere to the lesion, particularly pronounced in the primary and secondary motor cortex (Fig. 3I–K). Interestingly, Parvalbumin fluorescence expression in the terminals of PV-interneurons impinging onto non-PV neurons in layers II/III of the contralateral hemisphere are lower in 6-OHDA injected animals (Fig. 3F). This can be the direct consequence of the decreased expression of Parvalbumin expression in PV long-range projection cells that have their bodies in the ipsilateral hemisphere. On the contrary, there is a tendency of increased PV-puncta impinging onto non-PV neurons in layer II/III of the injected hemisphere that resulted significantly in M1 possibly indicating a reinforcement of PV projections from the contralateral hemisphere. This is in line with 3D dendritic reconstructions and Sholl analysis of PV-INs in the primary motor cortex which revealed a significant reduction in dendritic branching in layer II/III of the ipsilateral hemisphere (Fig. 3N). In contrast, PV-INs in the contralateral hemisphere display increased dendritic branch complexity (Fig. 3N). These findings suggest a shift in inter-hemispheric control, with the contralateral hemisphere compensating for functional deficits by enhancing long-range connectivity and synaptic integration.

PV-INs in cortical layers II/III possess relatively long axons that contact excitatory (pyramidal) and PV^+ cells, facilitating the synchronization of gamma oscillations[13]. These synchronized oscillations are integral to motor planning and execution and suggest a potential indirect influence on interhemispheric communication through long-range pyramidal neurons, particularly in layers II/III[64].

Recent experiments on brain slices of mice with 6-OHDA induced lesion in the medial forebrain bundle (MFB) suggest that layer V PV-INs in M1, when marked with td-Tomato viral expression, don't show any change in number, morphology and membrane properties[65]. This is in line with our findings suggesting that the overall cell numbers don't change in 6-OHDA mice while the expression of the Parvalbumin protein in the cell body and in the puncta-rings results altered. This can imply that dopaminergic loss may

alter calcium-binding properties in PV-INs, thus inducing an impaired local and long-range connectivity and, consequently, an imbalance in cortical oscillations.

Such changes in PV-IN distribution and synaptic activity highlight a broader disruption in the inhibitory network, extending beyond PV-IN cell bodies to their synaptic targets. This disruption likely compromises inhibitory control mechanisms, impairing the generation and maintenance of gamma oscillations that are crucial for cortical network stability. These structural alterations align with functional connectivity deficits, emphasizing the essential role of PV-IN integrity in maintaining cortical stability. Moreover, our findings contribute to a broader understanding of cortical dysfunction in PD models by highlighting the intricate relationship between neuronal density and synaptic adjustments in the regulation of cortical network stability.

Overall, our results suggest that dopaminergic loss does not lead solely to a breakdown of PV-IN-mediated cortico-cortical communication but instead triggers an asymmetric gain-of-function adaptation in the contralateral hemisphere, likely serving as a mechanism to offset motor and sensory deficits.

Atrophy of dendrite branching points in the ipsilateral hemisphere of 6-OHDA mice and the structural reorganization following degeneration of the dopaminergic system and consequent decrease of subcortical innervation to motor cortex are compensated with an enhanced synaptic strength. Globally, the observed symmetric reductions in PV cell bodies could reflect a widespread vulnerability of these neurons. Locally, within the ipsilateral hemisphere, the reduced connectivity among PV-PV circuits and the decrease in dendritic complexity may limit PV-IN functionality, potentially impairing inhibitory control mechanisms. This could necessitate compensatory synaptic remodeling, such as increased PV-to-non-PV connections. These changes might contribute to cortical network instability and altered oscillatory activity, potentially exacerbating motor deficits characteristic of Parkinson's disease.

The observed changes are consistent with previous reports of PV-IN vulnerability in neurodegenerative conditions[66,67] and underscore their importance as therapeutic targets in PD. The loss of PV-INs, which plays a central role in maintaining excitatory/inhibitory balance, may exacerbate cortical hyperexcitability and contribute to the E/I imbalance observed in this study. Indeed, histological analysis revealed a profound imbalance between excitatory and inhibitory synaptic markers[68,69] with increased excitatory drive likely compensating for dopaminergic loss in primary motor cortex. While VGAT levels (inhibitory synaptic marker) remained stable, VGLUT1 and VGLUT2 (excitatory synaptic markers) were significantly upregulated (Fig. 5A–F). Notably, the marked decrease in the PV expression of synapses impinging onto non-PV neurons doesn't alter VGAT expression levels, possibly indicating compensatory mechanisms involving several components of the inhibitory network. Moreover, our results show an increase in VGLUT1/2 perisomatic expression of synaptic puncta encircling individual neuronal somata. This focused analysis enables us to specifically assess axo-somatic synaptic contacts, which are critical for modulating neuronal output, in contrast to broader whole-field approaches[9,25] that encompass diverse synaptic types. This imbalance exacerbates cortical hyperactivity and disrupts normal motor processing. This suggests that cortical hyperactivity emerges as a compensatory response to subcortical degeneration. Interestingly, this E/I imbalance cannot be attributed to dopaminergic degeneration alone, as the motor cortex does not receive direct dopaminergic innervation[70,71]. Instead, we propose glutamatergic modulation plays a critical role, as the primary motor cortex integrates subcortical inputs and modulates striatal dopaminergic neurons[72–74].

In addition to neuronal and synaptic changes, we observed significant alterations in microglial activity in the motor cortex. Microglial cells displayed increased phagocytic activity, suggesting an ongoing neuroinflammatory response (Fig. 5G–I). Interestingly, we found an increase in VGLUT1 phagocytosis by microglia, which is captivating since total VGLUT1 in the tissue seems to be elevated. This apparent paradox may be explained by a compensatory upregulation of excitatory synapse formation in response to increased microglial activity, suggesting that neurons might bolster synaptic connectivity to offset potential losses. Alternatively, the accumulation of VGLUT1 could indicate that engulfed material is not fully degraded, thereby contributing to the overall increase. These findings underscore a dynamic interplay between synaptic remodeling and microglial clearance, hinting that heightened synaptic turnover may underlie the observed neurophysiological alterations. Such a scenario suggests a dynamic interplay between compensatory synaptic remodeling and neuroinflammatory processes, which may simultaneously exacerbate neuronal damage while attempting to preserve cortical functionality[75–77]. While this response may initially aim to clear debris and maintain homeostasis, excessive microglial activation could ultimately exacerbate cortical dysfunction and contribute to disease progression. Moreover, although we cannot yet definitively distinguish between E–E and E–I alterations, the elevated microglial engulfment of VGLUT1 supports active remodeling of excitatory synapses, consistent with pathology-induced plasticity. These insights emphasize the need to address both neuronal and microglial contributions in future therapeutic strategies.

Collectively, our findings point to a cascade of maladaptive cortical processes initiated by subcortical dopaminergic degeneration. Epsilon cortical hypersynchrony and pathological striatal delta modulation disrupt cortico-striatal communication, impairing motor control. Reduced PV-IN density and connectivity destabilize cortical networks, leading to hyperexcitability and compensatory plasticity, with hyper-synchronized activity and a possible overcoming of the contralateral hemisphere. PV alterations disrupt E/I balance and microglial phagocytosis amplifies synaptic turnover, linking neuroinflammation to synaptic remodeling and further circuit dysfunction. This cascade underscores the complex interplay between neuronal, synaptic, and inflammatory mechanisms in PD pathology. Taken together, these disruptions in local and global network dynamics contribute to motor deficits in PD. The progressive nature of these alterations emphasizes the importance of early intervention to prevent or mitigate cortical dysfunction.

Our combined use of principal component analysis (PCA) and support vector machine (SVM) classification (Fig. 4) enabled us to extract meaningful patterns from a high-dimensional dataset and to identify the variables most strongly associated with group differences. Notably, measures of functional connectivity emerged as top contributors in the PCA loadings (Fig. 4B) and were sufficient in training a SVM classifier able to discriminate between the two experimental conditions. This suggests that functional connectivity is not only a robust descriptor of underlying pathological states but also a potential biomarker for disease progression. Importantly, functional connectivity measures can be assessed longitudinally and, in some cases, non-invasively making them particularly attractive for use in preclinical therapeutic studies. Such data-driven approaches may help prioritize which parameters to monitor when evaluating the efficacy of interventions aimed at alleviating Parkinsonian symptoms in preclinical models.

Our results suggest that wide-field calcium imaging could serve as a valuable biomarker for monitoring disease progression and evaluating therapeutic efficacy (Fig. 4). The observed functional reorganization and both electrophysiological and synaptic imbalances provide critical insights into cortical compensatory mechanisms, reinforcing the need for targeted therapeutic strategies focused on the motor cortex. By impairing gamma oscillations and long-range synchrony, PV-IN reductions likely disrupt motor planning and execution, hallmark features of PD pathology. Future therapeutic strategies should focus on restoring PV-IN function or compensating for their loss to stabilize cortical networks and improve motor outcomes in PD. Non-invasive approaches, such as transcranial alternating current stimulation, might offer promise for modulating abnormal cortical activity and synchronizing cortico-striatal circuits[78]. Additionally, altered microglial activity suggests that neurotrophic factors, such as nerve growth factor (NGF), may help restore neuronal function and mitigate neuroinflammation[79]. In conclusion, addressing motor cortex dysfunction

is essential for slowing PD progression and improving motor function. A combination of therapeutic approaches, such as brain stimulation to correct electrophysiological abnormalities and NGF to support neuronal survival, might offer a synergistic path forward.

While this study provides valuable insights into the 6-OHDA mouse model of Parkinson's disease, several limitations must be acknowledged. The 6-OHDA model successfully recapitulates key aspects of dopaminergic neuron loss; however, it does not fully capture the progressive and bilateral nature of human PD. In this study, we utilized a unilateral lesioning approach to establish a well-characterized model of pathology. Nevertheless, exploring bilateral lesion models in future studies could be useful for assessing therapeutic efficacy in a more widespread neurodegenerative context, thereby improving the translational relevance of clinical applications. This said, the imaging and immunohistochemical data involving the contralateral hemisphere may possibly have important implications regarding a compensatory or maladaptive remodeling of circuitry in one of the two hemispheres that can be less affected or in a earlier stage of the pathology with respect to the others. However, deeper investigations are necessary to dissect this hypothesis. In the same line, it is important to note that the observed reduction in inter-hemispheric, but not intra-hemispheric, coherence may in part reflect the effects of the unilateral 6-OHDA lesion. While this could be viewed as a model-specific artifact, it is also consistent with the clinical presentation of PD, which often begins asymmetrically with lateralized motor symptoms and inter-hemispheric differences in neural activity[80,81]. The unilateral lesion model is widely used to capture this early-stage asymmetry, providing a relevant framework for investigating disrupted network dynamics. Nonetheless, we acknowledge that the unilateral nature of the lesion may itself contribute to the coherence changes observed, and future studies using bilateral models or longitudinal approaches are warranted to determine the extent to which inter-hemispheric dysregulation reflects core pathophysiology versus model-specific effects.

Additionally, this study primarily focuses on motor deficits, while non-motor symptoms, such as cognitive and emotional dysfunctions, remain unexplored. Since our objective was to investigate the motor cortex as a potential therapeutic target, we employed a model that effectively reflects motor symptoms. However, incorporating assessments of non-motor dysfunctions in future studies would provide a more comprehensive understanding of the disease. On the other hand, despite the novelty represented by the retraction task on the M-Platform, the behavioral phenotype associated with these cortical rearrangements should be investigated more deeply, looking for finer motor alterations. For this purpose, other custom-made behavioral platforms are in development in our lab to assure a direct correlation between circuital remodeling and motor function.

Furthermore, longitudinal studies could be valuable for elucidating the chronic effects of dopaminergic degeneration. Another consideration concerns the interpretation of cortico-striatal dynamics, as this study does not establish a direct causal relationship between the cortex and striatum. This limitation suggests the need for further exploration of multisynaptic pathways or shared synaptic drives to better explain the observed findings.

While the origin of the ~4 Hz LFP peak remains uncertain, and may partially overlap with physiological rhythms such as respiration or heart rate, we believe this is unlikely to be a major confound given our use of bipolar recordings and the consistency of this finding with previous reports in Parkinsonian mice[35]. Nonetheless, future studies combining LFPs with simultaneous respiratory and ECG monitoring will be necessary to systematically rule out contamination from non-neural sources.

Although we observed significant correlations between cortical epsilon power and both behavioral performance and dopaminergic degeneration markers (Supplementary Fig. 3C–F), our limited sample size prevented us from performing a formal mediation analysis. Such analyses require a larger number of subjects to ensure sufficient statistical power and reliability. Therefore, we consider these initial correlations exploratory. Future studies with expanded sample sizes will be necessary to formally test the mediation model and to further clarify whether causal relationships exist between dopaminergic degeneration, cortical epsilon activity, and motor deficits in the 6-OHDA model.

Finally, although the results highlight potential therapeutic targets, such as non-invasive brain stimulation and nerve growth factor (NGF)-based interventions, further investigations in more complex preclinical models or clinical settings are required to validate these approaches before their translation into human therapies.

Methods

Animals

Adult wild-type male C57BL/6J mice (3–4 months old; RRID: IMSR_JAX:000664) were used for electrophysiological and histological analyses ($n = 8$ CNT and $n = 13$ 6-OHDA). Adult homozygous male PV-Cre knock-in mice (2–3 months old; RRID: IMSR_JAX:008069), were used for wide-field imaging analysis and histological analyses ($n = 5$ CNT and $n = 4$ 6-OHDA). Only male mice were included in the study in order to maintain clarity and avoid confounding effects based on evidence of sex differences in PD pathophysiology between male and female subjects reported by the literature. Mice were housed up to four animals per cage under a 12-h/12-h light/dark cycle with access to food and water ad libitum. All experimental procedures respected the ARRIVE guidelines and the European Communities Council Directive #86/609/EEC were approved by the Italian Ministry of Health Autorizzazione no. 544/2023-PR (Risp. a prot. B4BB8.43). Animal numbers were minimized in line with the 3Rs principle, particularly Reduction, to ensure ethical use of animals while maintaining sufficient statistical power. The use of wide-field calcium imaging in awake, head-fixed mice with chronic cranial windows during behavioral tasks necessitated technically demanding and longitudinal protocols. Accordingly, within-subject experimental designs and repeated imaging sessions were employed to maximize data yield per animal and reduce inter-individual variability. Sample sizes were informed by prior studies and pilot data to balance scientific validity with ethical considerations. Animal welfare was monitored by both the research team and the animal facility staff using observation protocols. Veterinary support from the facility ensured timely intervention in case of abnormal signs related to health and welfare. Welfare assessment included checks for food and water intake, behavior, specific facial expressions, piloerection and abnormal posture.

6-OHDA injection

To induce a Parkinsonian model, intra-striatal injections of 6-hydroxydopamine (6-OHDA) were performed. Mice were anesthetized with ketamine (100 mg/kg) and xylazine (10 mg/kg) and placed in a stereotaxic frame. The right striatum was targeted using the following coordinates relative to bregma: anterior-posterior (A/P) + 1.0 mm, mediolateral (M/L) −1.8 mm, and dorsoventral (D/V) −3.2 mm. A Hamilton syringe with a fine glass capillary was used to inject 6 mg/mL 6-OHDA dissolved in ascorbic acid solution (0.02% mg/mL) in sterile saline at a rate of 0.2 µL/min for a total volume of 2 µL[17,82,83]. Control mice received the same volume of physiological saline and ascorbic acid solution.

Electrophysiological recordings

Surgery. Stainless steel bipolar electrodes were implanted immediately following the 6-OHDA injection. The striatal electrode, targeting the striatum (CPu), was positioned at the same coordinates as the toxin injection (coordinates relative to bregma: anterior-posterior (A/P) + 1.0 mm, mediolateral (M/L) −1.8 mm, and dorsoventral (D/V) −4 mm). The cortical electrode was inserted 1 mm posterior to the striatal electrode, maintaining the same mediolateral coordinate. This cortical electrode was 1 mm in length, sufficient to reach the superficial layers of the primary motor cortex (M1). An additional hole was drilled at the center of the occipital bone to facilitate the insertion of a surgical screw, which served both as a ground reference and to provide additional stability to the recording implant. The two bipolar electrodes were then soldered to the pins of a connector. The ground pin was connected to the

occipital screw, and a first layer of dental cement (Super Bond CeB, Sun Medical Co., Japan) was applied to secure all components to the skull surface. Once the first layer of cement had dried, a second layer (Paladur, Pala, Germany) was applied to enclose the electrical components. To assure a proper head fixation of the animal, crucial for task performance and signal quality during recordings, an L-shaped metal bar (0.6 g) was also attached to the occipital bone using dental cement Super Bond. Following surgery, glucose and paracetamol were administered, and the mice were allowed to recover. After all surgical procedures, animals were carefully stitched and treated with intra-operative analgesia (tramadol 10 mg/kg) and intramuscular injection of cortisone (Bentelan 0.05 ml) upon waking from anesthesia. As a further analgesic, paracetamol (100 mg/kg) was administered for 4 days post-operation in drinking water. The implant enabled simultaneous recordings of neuronal activity in the striatum and motor cortex of the ipsilateral hemisphere relative to the dopaminergic lesion. Electrophysiological recordings were performed during both rest and motor tasks, beginning in the first week post-lesion and continuing until the fourth week. Particular attention was given to monitor head fixation procedure, considering the possible effect of stress on cortical activity. The acclimatation phase it is made easier with the use of a sweet reward given randomly and independently from the retraction task. As described in Spalletti et al.[19], mice are able to quickly associate the retraction task to the reward and already after 2 to 3 days they enter spontaneously in the cage for head fixation. The animals' stress levels and any signs of discomfort were monitored both during the acclimatization phase and throughout the experimental phase. In the event that signs of distress were identified during the experiment, the cause was immediately addressed and eliminated whenever possible (e.g., uncomfortable positioning of the animal, discomfort due to inappropriate lighting or noise in the room, etc.). If the cause could not be resolved, the experimental session was interrupted. At the end of the experiment, each animal was returned to its home cage with the other animals, after the head cap was removed.

Recordings. Neuronal activity from each bipolar electrode was acquired through a miniature headstage (NPI, Germany) connected to a 2-channels extracellular amplifier (EXT-02F, NPI). Signals were amplified (10.000-fold), filtered (high pass 0.3 Hz; low pass, 300 Hz), digitized with a sampling rate fs = 1 KHz (National Instruments Card), and conveyed to a computer for a storage and analysis.

M-Platform for forelimb retraction task. The M-Platform is a robotic system developed in our laboratory for upper limb exercise in mice[19,84].It consists of a linear actuator (Micro Cylinder RCL, IAI Germany), a 6-axis load cell (Nano 17, ATI Industrial Automation USA) with a controlled friction system, and a custom-designed handle fixed to the left forelimb positioned on a precision linear sled (IKO BWU 25-75, USA). One end of the handle is screwed onto the load cell for force transfer to the sensor, while the other end serves as a support for the animal's wrist[20].

Electrophysiological recordings at rest. After 24 h of recovery, mice were acclimated to the head restraining system on the M-Platform. Weekly training sessions were conducted for both resting-state and motor task recordings. For resting-state recordings, mice were head-fixed on the M-Platform, with the left forepaw linked to the load cell but without performing the forelimb retraction task. This configuration minimizes voluntary movements, allowing the acquisition of neuronal activity exclusively in the ipsilateral hemisphere during rest and excluding any movements sensed by the M-Platform. The chronic recording setup included two bipolar electrodes for simultaneous local field potential (LFP) recordings in the striatum and motor cortex. Signals were amplified using a DigiAmp (Plexon, USA) and referenced to a ground electrode placed at the cerebellum. Data acquisition was performed using the OmniPlex D Neural Data Acquisition System (Plexon Inc., USA). Resting-state signals were recorded for 3 min in an awake but stationary state.

Electrophysiological recordings during voluntary motor task. Following the resting-state recordings, mice performed the forelimb retraction task, during which LFP signals from the striatum and motor cortex were recorded. Each session consisted of 15 forelimb retractions, alternating between passive (device-extended by 10 mm) and active (animal-retracted) movements. A sugar water reward was provided for each successful task completion, contingent on surpassing a defined force threshold. Mice typically mastered the task within 2–3 days[19]. Task friction was adjusted based on individual functional deficits. Electrophysiological signals were recorded throughout the task to capture neural activity in the ipsilateral hemisphere during the motor performance. A high-resolution camera (Zyno Full HD, Trust Netherlands, 25 Hz) was positioned parallel to the coronal plane of the animal, capturing video footage synchronized with load cell force signals. Position and velocity signals were extracted from the video and aligned with force signals using a custom algorithm developed in Matlab (MathWorks, USA)[19]. NeuroExplorer software was used to process power spectral density (PSD) data during the task and LFP signals associated with force peaks. Offline analyses, performed with custom algorithms in NeuroExplorer and Matlab, included PSD computation and synchronization of neural and force signals. This setup enabled detailed analysis of cortical and striatal activity during both resting and motor task conditions, providing insights into the neuronal dynamics associated with the lesion-induced motor deficits.

Electrophysiological recordings data analysis

LFP extraction and spectral analysis at rest. From extracellular recordings during the resting state, local field potentials (LFPs) were extracted by applying a low-pass filter at 200 Hz. The LFP signals were then *z*-scored prior to spectral analysis to normalize the data. Recordings with excessive signal deflection exceeding ±5 SD of the mean were removed from further analyses. The power spectral density (PSD) of the *z*-scored LFPs was calculated using the Fast Fourier Transform (FFT) implemented via the Welch method (using the pwelch function in MATLAB). For this analysis, the time window of interest was divided into 10-s sub-windows with 50% overlap to improve spectral estimation. Frequency bands of interest were defined as follows: delta (2.5–5.5 Hz), beta (13–30 Hz), gamma (30–60 Hz), and high-gamma (60–100 Hz), and their respective power was computed as the average PSD within these frequency ranges. For the resting-state analysis we excluded from the LFPs those signals' portions contaminated by animal movements.

To isolate oscillatory power from the aperiodic background in the LFP spectra, we used the Fitting Oscillations and One-Over-F (FOOOF) algorithm[18] with a maximum of 15 peaks, fit over the 0–200 Hz range. For each animal and brain region, we extracted the aperiodic fit from the log-log transformed PSD. To normalize the PSD, we first reconstructed the aperiodic component in linear space and then subtracted and divided the raw PSD by this background fit: normalized PSD = (raw PSD – aperiodic fit)/aperiodic fit.

The boundaries of the delta band were determined empirically based on the spectral properties of our data, which exhibited a prominent low-frequency peak centered around ~4 Hz across both cortical and striatal LFPs. While the 4 Hz peak lies near the boundary typically separating delta and theta rhythms, we refer to this range as "delta" in line with previous work in the mouse basal ganglia, particularly in dopamine-depleted conditions[35,85,86]. It is important to note that frequency band classifications are not universally fixed and may vary depending on species, brain region, and experimental context. Here, the term "delta" is used as a descriptive convention to capture the dominant low-frequency (below 5.5 Hz) activity observed in our data, rather than to imply a strict physiological distinction.

Coherence analysis at rest. The magnitude-squared spectral coherence between striatal and cortical LFPs was estimated using the mscohere

function in MATLAB. This function computes the coherence as the ratio between the magnitude-squared cross-power spectral density of the two signals and the product of their individual PSDs.

Cross-correlation of delta power fluctuations at rest. To investigate functional connectivity, we computed the cross-correlation between delta power fluctuations of the striatal and cortical LFPs using the xcorr function in MATLAB. Delta power fluctuations were estimated by applying a Hilbert transform to the delta-filtered (4th-order Butterworth bandpass filter using Matlab's *filtfilt* function to ensure zero-phase distortion) signal and then taking the absolute value of the resulting signal to obtain the envelope of the delta activity.

Time-frequency analysis of motor task LFPs. To analyze the temporal evolution of spectral patterns in LFPs during motor tasks, we performed time-frequency decomposition using wavelet analysis. LFP scalograms) were generated via continuous wavelet transform (MATLAB *cwt* function) with the analytic Morse wavelet, setting the symmetry parameter to 3 and the time-bandwidth product to 60 for optimal resolution. The entire LFP recording was subjected to wavelet transformation, and the resulting time-frequency scalograms were segmented into windows spanning from −1500 ms to +500 ms relative to movement onset. For normalization, scalograms were baseline-corrected using a reference period between −1500 ms and −750 ms before movement onset. We specifically examined movement-related power modulation in the delta (2.5–5.5 Hz) and epsilon (100–150 Hz) frequency bands. These were extracted from the scalograms within the [0, 250 ms] window post-movement onset to capture task-related neural activity.

M-Platform parameters extraction for motor task. the M-platform parameter extraction was calculated as previously shown in Grealish et al.[19]. Briefly, task-related variables were derived from position, speed, and force signals, including the mean force, calculated as the average force from peaks detected during sub-movements, and the area under the force curve (AUC), which represents the total force exerted over time during movement.

Wide-field imaging

Surgery. PV-Cre mouse line, in which Cre recombinase is selectively expressed under the control of the parvalbumin (PV) promoter, underwent wide-field imaging. For parvalbumin-expressing interneurons (PV-INs) labeling with GCaMP7f, the Cre-dependent viral construct ssAAV-PHP.eB/2-hSyn1-chl-dlox-jGCaMPf(rev)-dlox-WPRE-SV40p(A) (1.3x10E13 vg/ml, volume: 50 µL, Viral Vector Facility, ETH, Zurich) was diluted in 100 µL of saline solution. A final volume of 150 µL was intravenously injected in the retro-orbital sinus of PV-Cre mice under isoflurane anesthesia at P60 to allow wide-brain infection[87]. Two weeks after AAV injection, mice were injected with either 6-OHDA ($n = 4$) to induce a parkinsonian model or vehicle ($n = 5$) for control conditions. Immediately following the injection, the mice underwent an intact-skull preparation to provide direct optical access to the cortex (modified from Montagni et al.[88]). The surgery was performed under a cocktail of ketamine/xylazine (100/10 mg/kg i.p.). The skin and the periosteum were removed. Bregma was marked for stereotactic reference. A custom-made aluminum head-bar placed behind lambda was glued to the skull using transparent dental cement (Super Bond C&B—Sun Medical). The exposed skull was then covered with a thin layer of the same cement.

Wide-field microscopy setup. Imaging was performed on the intact skull of the awake head-fixed animal using a custom-made microscope setup. To excite the GCaMP7f indicator, a 470 nm light beam (LED, M470L3, Thorlabs) filtered by a bandpass filter (469/17.5 nm, Thorlabs) is directed by a dichroic mirror (MD498, Thorlabs) onto the objective lens (TL2X-SAP 2X Super Apochromatic Microscope Objective, 0.1 NA, 56.3 mm WD, Thorlabs). The fluorescence signal was selected by a bandpass filter (525/50 nm filter, Semrock, Rochester, New York, USA) and collected by a CMOS camera (ORCA-Flash4.0 V2 Digital CMOS camera/C11440-22CU, Hamamatsu). Images are acquired with 9 ms exposure time in External Edge mode at 50 Hz for 6000 total frames with a resolution of 512 × 512 pixels and a field of view (FOV) of 1.15 × 1.15 cm (depth 16-bit).

Habituation and awake imaging. One week after the surgery mice were acclimated to the head-fixation for 5–4 days (10 min a day/mouse) to gradually reduce anxiety and abrupt movements prior to data collection. Head-fixed imaging sessions were performed at 14, 21 and 28 days post lesion (DPL). Each imaging session involves 5 recordings (180 s-long) of spontaneous cortical activity in awake, resting-state mice.

Image processing and data analysis. All analyses were performed in MATLAB. Each imaging session was registered using custom-made software, by taking into account the bregma and λ position. An animal-specific field of view template was used to manually adjust the imaging field daily. To dissect the contribution of each cortical area, we registered the cortex to the surface of the Allen Institute Mouse Brain Atlas (www.brain-map.org) projected to our plane of imaging. For each block, image stacks were processed to obtain the estimates of $\Delta F/F0$. $\Delta F/F0$ was computed for each pixel by using the equation $\Delta F/F0 = (F–F0)/F0$, with F representing fluorescence at a given time and F0 the mean fluorescence[88,89]. The field of view was then downsampled to 128 × 128 pixels. Global signal regression (GSR) was applied and a total of 22 ROIs were then selected (11 ROI for each hemisphere, 5 × 5 pixels) representing key cortical regions. Correlation mapping was done for each subject by computing Pearson's correlation coefficient between the average signals extracted from each ROI, with that of each other ROI. The single-subject correlation maps were transformed using Fisher's r-to-z transform and then averaged across all animals. Average maps were re-transformed to correlation values (r-scores) for figure purposes. For each mouse, r(CNT)-r(6-OHDA) was calculated and averaged across mice in order to visualize matrices of difference between mice injected with vehicle or 6-OHDA.

The abbreviations and extended names for each areas are as follows: MOs-a, anterior region of secondary motor cortex; MOs-p, posterior region of secondary motor cortex; MOp-a, anterior region of primary motor cortex; MOp-p, posterior region of primary motor cortex; SSp-bfd, primary somatosensory area, barrefield; SSp-tr, primary somatosensory area, trunk; SSp-fL, primary somatosensory area, forelimb; SSp-hl, primary somatosensory area, hindlimb; RSP, retrosplenial cortex; VISa, associative visual cortex; VISp, primary visual cortex. Throughout the text and figures, suffixes L and R were added to denote cortical areas of the left or right hemisphere, respectively (e.g., RSP_L, RSP_R).

Statistical analysis. Network Based Statistic (NBS) Toolbox in MATLAB was used to statistically assess functional network connectivity[90,91]. We tested for both significantly higher and lower correlations. Differences were considered significant at $p < 0.05$.

Schallert Cylinder Test

The Cylinder Test was conducted weekly starting from the first week post 6-OHDA injection to assess disease progression[83]. The Cylinder Test is highly effective for assessing unilateral sensorimotor and motor dysfunctions. Animals are placed inside a Plexiglas cylinder (8 cm in diameter, 15 cm in height) adapted for mice according to the protocol described by Schallert and Tillerson[92]. Each animal is recorded for 5 min using a camera (SMXF50BP/EDC, Samsung, Seoul, South Korea) positioned beneath the cylinder. Videos are analyzed frame by frame to count the number of each forepaw touches on the cylinder wall. A detailed scoring protocol was followed, based on established definitions of forelimb placements during rearing. Specifically, the first paw touch on the cylinder walls and the subsequent placement of the forelimbs back on the cylinder base are recorded[84].

To ensure accuracy and reliability, scorers were blinded to experimental groups to prevent bias and two independent observers scored the videos with inter-rater reliability assessed to ensure consistency. To quantify the number of touches made with the limb contralateral to the injection site, the % Contralateral Forelimb was calculated as the ratio of the number of touches made with the forelimb contralateral to the lesion while the animal climbs vertically within the cylinder to the total number of touches[93]. Importantly, all values were normalized to each animal's own pre-surgery baseline performance, allowing us to detect changes in asymmetry over time and account for individual variability in initial motor behavior.

Histology

Mice were deeply anesthetized with chloral hydrate and perfused transcardially with 4% paraformaldehyde (PFA, Electron Microscopy Sciences) in 0.1 M phosphate buffer. Extracted brains were post-fixed in 4% PFA for 2 h, followed by 30% sucrose in phosphate buffer at 4 °C. Brains were sectioned coronally at 50 µm using a sliding microtome (Leica, Germany) and maintained in PBS for free-floating immunostaining.

For immunostaining, brain slices were incubated in a blocking solution for 1 h at room temperature (10% donkey serum; 0.3% Triton X-100 in PBS), treated with primary antibodies, prepared at the proper concentration in 1% donkey serum and 0.2% Triton X-100 in PBS overnight at 4 °C. Following 3 washes in PBS, the sections were incubated for 2 h at room temperature with the specific secondary antibodies. For nuclei visualization Hoechst dye (#B2883; 1:500; Bisbenzimide, Sigma Aldrich, USA).

Immunohistochemical analysis was conducted on the substantia nigra pars compacta and striatum using primary anti-tyrosine hydroxylase (1:500 TH, INVITROGEN PA5-85167) and corresponding secondary antibodies for detection of unilateral dopamine degeneration and confirm lesion presence. All the analyses on PV-IN were performed through immunohistochemical labeling with anti-parvalbumin primary antibody, PV (1:500, SYSY 195 004). Cortical plasticity markers such as vesicular glutamate transporter type 1, VGLUT1 (1:500, SYSY 135 304); vesicular glutamate transporter type 2, VGLUT2 (1:500, SYSY 135 403); and vesicular GABA transporter, VGAT (1:500, SYSY 131 005) were also investigated in primary motor cortex, particularly vesicular markers in superficial layer II/III. Microglial cells and phagosomes in the cortex were stained respectively with rabbit anti-Iba1 1:500 (Wako, Osaka, Japan, 019–19741) and rat anti-CD68 1:250 (BioRad, #MCA1957).

Dopaminergic lesion analysis. TH^+ fibers signal was acquired using a Zeiss Axio Observer microscope equipped with a Zeiss AxioCam MRm camera (Carl Zeiss MicroImaging GmbH, Germany). For each tissue slice, images were captured with a 10x objective and stitched into a single composite image using Zen Blue Edition software (Carl Zeiss MicroImaging GmbH, Germany). Relative Optical Density (ROD) analysis was performed on 8-bit converted images using ImageJ software (National Institutes of Health, USA) to quantify the mean fluorescence of dopaminergic fibers in the striatum, based on a calibration curve. Quantification of TH-positive neurons in the substantia nigra was conducted using Neurolucida software (MBF Bioscience).

Cortical vesicular markers analysis. High-resolution z-stack images (5 stacks, z-step 0.17 µm) of cortical sections immunostained for vesicular markers of excitatory (VGLUT1, VGLUT2) and inhibitory (VGAT) neurons were acquired using a Zeiss LSM 880 Airyscan Confocal Microscope (Carl Zeiss MicroImaging GmbH, Germany), equipped with a 63× oil immersion objective and a 1.3× digital zoom to enhance resolution. The acquisition parameters were kept constant across samples to ensure data comparability. To analyze synaptic marker distribution, we employed an ImageJ-based automated workflow adapted from previously validated protocols[94–98]. We defined regions of interest (ROIs) surrounding individual cell bodies (perisomatic area) to selectively assess synaptic puncta-ring intensity and detect changes in the expression of synaptic markers. Mean fluorescence intensity of the identified synaptic puncta was measured within these ROIs, and the signal from the somatic area was subtracted to correct for background and nonspecific staining.

This perisomatic quantification allows for spatially resolved analysis of synaptic inputs specifically targeting neuronal cell bodies—a strategy designed to capture functional changes in synaptic connectivity that may be overlooked by field-wide analysis.

To assess the functional contribution of PV interneurons (PV-INs), we further analyzed the mean fluorescence of PV-positive puncta specifically surrounding non-PV neuronal somata in M1, M2 and S1BF. These regions were selected based on prior wide-field imaging that identified hypo-connected cortical areas in the 6-OHDA mouse model. For each hemisphere, a minimum of three non-overlapping fields of view from three brain sections per animal were acquired. Within each field, at least three clearly identifiable neuronal somata were analyzed, resulting in a minimum of $n = 216$ cells per synaptic marker across all experimental conditions. Data from the ipsilateral hemisphere were normalized to the contralateral side (internal control) to minimize inter-sample variability and account for potential systemic fluctuations in staining or imaging.

In addition we performed an automated pipeline using the plugin "Analysing Particles" in ImageJ software (National Institutes of Health, USA) for the quantification of the percentage of the area of puncta respect to the area of the field of view (FOV), the mean fluorescent of all the FOV, and unbiased stereology for the quantification of synaptic markers PV, VGAT, VGLUT1 and VGLUT2 puncta in the layer II/III of M1. Specifically, synaptic puncta were counted in each brain section using a grid size of 250 × 850 µm and a counting frame of 77 × 77 µm. The density of synaptic markers was estimated on the basis of the immunostaining signals between 5 and 8 µm below the surface of slices using the optical dissector method. Brain slices were 50 µm thick, and one out of every four sections was sampled (Section Sampling Fraction = 1/4). All stereological analyses were conducted by an operator blinded to genotype. Images were acquired using a Zeiss Airyscan confocal microscope (Carl Zeiss MicroImaging GmbH, Germany) and a Plan-Apochromat 63x/1.40 Oil DIC M27 objective and a 1.3 digital zoom, using identical acquisition settings (1572 × 1572 pixels; 0.85 µm depth; 0.17 µm z-step).

PV-IN and NeuN density. PV^+ and neuronal cell bodies were identified through anti-parvalbumin (PV, 1:500, SYSY 195 004) and anti-NeuN (Neuen,1:500, SYSY 266 006) immunohistochemistry respectively and analyzed across three cortical regions—M1, M2, and S1BF—using anatomical alignment based on the Allen Brain Atlas. Image acquisition was conducted using a Zeiss Axio Observer microscope equipped with a Zeiss AxioCam MRm camera (Carl Zeiss MicroImaging GmbH, Germany) and a 10× objective, with identical acquisition settings applied to all images. For each section, a single focal plane was captured from the central portion of the tissue to optimize visualization and reduce edge-related artifacts. Automated total cell counting was performed across the full extent of each target area within individual sections, following precise anatomical references to ensure consistency across samples. Quantification of PV^+ and $NeuN^+$ neurons was specifically carried out within cortical layers II/III of each region, guided by Hoechst nuclear staining to delineate laminar boundaries. For each animal, four serial coronal sections were analyzed—each 50 µm thick and spaced 200 µm apart—allowing for representative sampling along the anterior-posterior axis of the selected cortical areas. Image analysis was performed using custom Python-based pipelines, including MicroNeuSeg[99] and CounTastic[100], ensuring high-throughput, unbiased, and reproducible detection of PV^+ cell bodies. All analyses were conducted by an experimenter blinded to the animal's genotype. For each subject, PV-IN and NeuN density for each slice was divided by the area multiplied by the thickness, allowing estimation of cell density in three dimensions. The final automated total PV^+ interneuron (PV-IN) counting with volumetric normalization was expressed as the number of PV^+ cells per cubic millimeter (cells/mm^3), providing a consistent and quantifiable measure of interneuron distribution across both cortical depth and region.

PV-IN morphology. PV-IN morphology was analyzed ex vivo in the motor cortex of PV-Cre mice injected with the Cre-dependent AAV-PHP.eB/2-hSyn1-chl-dlox-jGCaMPf(rev)-dlox-WPRE-SV40p(A) virus, following wide-field imaging. The robust GFP signal expressed by the virus enabled detailed visualization and analysis of small dendrites and all neurons co-localizing with PV^+ cells. Confocal z-stacks spanning approximately 40 µm were acquired with a z-step of 0.23 µm, resulting in a final voxel size of $0.31 \times 0.31 \times 0.23$ µm. Images were subsequently processed using the Filament Tracer Tool of IMARIS software (Bitplane) for semi-automatic three-dimensional reconstruction and quantitative morphometric analysis. For each hemisphere and analyzed mouse, approximately 10 PV^+ cortical neurons were reconstructed, allowing for a detailed assessment of dendritic architecture and cellular morphology.

Microglia analysis. for microglial density analysis, 1024×1024 pixel images were acquired with a confocal microscope (Stellaris 8 confocal microscope, Leica microsystems) using a 20x objective (HC PL APO CS2, 20x/0.75 DRY), and pinhole was set to 1 AU. Sequential illumination with 488 nm laser lines was used to detect Iba1. The central plane of the sample in the *z*-axis was selected for image acquisition. Images were processed through Fiji Image software: microglia somata and areas of brain regions (in µm) were counted by combining the Cell Counter and selection of ROI options. For each subject, Iba1 density for each slice was divided by the area multiplied by the thickness, allowing estimation of cell density in three dimensions. The final automated total PV^+ interneuron (PV-IN) counting with volumetric normalization was expressed as the number of $Iba1^+$ cells per cubic millimeter (cells/mm^3), providing a consistent and quantifiable measure of interneuron distribution across both cortical depth and region.

For the quantification of engulfed materials, 1024×1024 pixel images were acquired with a confocal microscope (Stellaris 8 confocal microscope, Leica microsystems) using a 63x oil objective (HC PL APO CS2 63x/1.40 OIL), and pinhole was set to 1 AU. Sequential illumination with 488 nm, 568 nm and 633 nm laser lines was used to detect VGLUT1, Iba1 and CD68, respectively. Importantly, Z stacking was performed for ~10–15 µm, with 0.5 µm steps in the z direction, selecting the most fluorescent VGLUT1 signal into the z direction, to optimize the detection of puncta. Analysis of engulfed and non-engulfed material was performed via 3D volume rendering in Imaris Bitplane software, as described in ref. 101. VGLUT1 engulfed in CD68 [(Volume of VGLUT1 in CD68/Volume of CD68)] / [Volume of Total Engulfed and Non-Engulfed VGLUT1/Volume of Field] and volume of $CD68^+$ phagosomes (Volume of CD68/Volume of Iba1) × 100.

For the quantification of engulfed materials, 1024×1024 pixel images were acquired with a confocal microscope (Stellaris 8 confocal microscope, Leica microsystems) using a 63x oil objective (HC PL APO CS2 63x/1.40 OIL), and pinhole was set to 1 AU. Sequential illumination with 488 nm, 568 nm and 633 nm laser lines was used to detect VGLUT1, Iba1 and CD68, respectively. Importantly, Z stacking was performed for ~10–15 µm, with 0.5 µm steps in the z direction, selecting the most fluorescent VGLUT1 signal into the z direction, to optimize the detection of puncta. Analysis of engulfed and non-engulfed material was performed via 3D volume rendering in Imaris Bitplane software, as described in Schafer et al.[101]. VGLUT1 engulfed in CD68 [(Volume of VGLUT1 in CD68/Volume of CD68)] / [Volume of Total Engulfed and Non-Engulfed VGLUT1/Volume of Field] and volume of $CD68^+$ phagosomes (Volume of CD68/Volume of Iba1) × 100.

Statistical analysis

Statistical analyses were performed using Prism software (GraphPad, USA). All values reported are the mean ± Standard Error of Mean (indicated in the caption). For all analyses, $\alpha = 0.05$. To determine the employment of statistical parametric or non-parametric tests, a normality test has been performed (Shapiro–Wilk test or Kolmogorov–Smirnov test). For electrophysiological experiments, the statistical significance of power, coherence, correlation, and power modulation was evaluated using a two-way ANOVA followed by Sidak's multiple comparisons test. The analysis included two factors: recording weeks and animal group (6-OHDA vs. CNT). The tests were applied to datasets containing multiple recordings per week across animals, without averaging data at the animal level prior to statistical analysis. To further explore differences between groups, post-hoc pairwise comparisons were conducted between the two animal groups at each recording week using the Wilcoxon rank-sum test, allowing for non-parametric evaluation of group differences. For behavioral test analysis a two-way repeated measures ANOVA followed by Sidak's multiple comparisons test was used to compare 6-OHDA vs. CNT and one sample *t*-test with Holm-Sidak's multiple comparisons for longitudinal intragroup studies with respect to the baseline. This choice was based on our dataset that is fully balanced with no missing values while the study design allowed repeated measurements from the same animals across time points. Given the small sample size, stable convergence, and the clear interpretability of main and interaction effects, repeated measures ANOVA was deemed appropriate.

For histological analysis a two-way repeated measures ANOVA followed by Sidak's multiple comparisons test was used to compare CNT contra, CNT ipsi, 6-OHDA ipsi, 6-OHDA contra.

PCA analysis

PCA analysis was performed on python (sklearn.decomposition.PCA) using as a dataset all the collected parameters for each animal (9 animals, 49 features including histology and functional connectivity data). Each feature's loading in PC1 was assessed by looking at pca.components_ and ranked.

Training of the SVM classifier. To identify potential biomarkers for classifying mice as diseased(6-OHDA) or non-diseased (CNT), we implemented a Support Vector Machine (SVM) classification approach using a leave-one-out cross-validation (LOOCV) strategy. The dataset used was the same as for *PCA Analysis*. Prior to classification, the features were standardized using sklearn.preprocessing.StandardScaler to ensure comparability and optimal performance of the SVM. To rigorously evaluate model performance and ensure unbiased estimation of classification accuracy given the low number of rows, we used LOOCV. In this approach, each mouse sample was sequentially left out as the test set while the remaining samples were used to train the SVM model. This process was repeated until every sample had been used once as the test set. The SVM classifier was thus trained using either the entire dataset (All), only histological parameters for puncta markers (Puncta), only histological parameters for lesion quantification—CPu TH^+ fibers and SNc TH^+ neurons—(Lesion), only functional connectivity data (FC). To validate the accuracy of the classification model, we generated a scrambled version of the dataset by randomly shuffling the class labels while keeping the feature data intact. The same LOOCV procedure was applied to this scrambled dataset to establish a baseline for comparison (bootstrap).

Data availability

All source data are accessible in a public database titled "Parkinsonism disrupts cortical function by dysregulating oscillatory, network and synaptic activity of parvalbumin positive interneurons" with its reference: DOI: 10.17632/r24brw4szj.1, accessible upon acceptance of the paper.

Received: 4 April 2025; Accepted: 13 June 2025;
Published online: 01 July 2025

References

1. Kouli, A., Torsney, K. M. & Kuan, W.-L. *Parkinson's Disease: Etiology, Neuropathology, and Pathogenesis* (Codon Publications, 2018).
2. DeMaagd, G. & Philip, A. Parkinson's disease and its management: part 1: disease entity, risk factors, pathophysiology, clinical presentation, and diagnosis. *P T* **40**, 504–532 (2015).

3. Moustafa, A. A. et al. Motor symptoms in Parkinson's disease: a unified framework. *Neurosci. Biobehav. Rev.* **68**, 727–740 (2016).
4. Lindenbach, D. & Bishop, C. Critical involvement of the motor cortex in the pathophysiology and treatment of Parkinson's disease. *Neurosci. Biobehav. Rev.* **37**, 2737–2750 (2013).
5. Magrinelli, F. et al. Pathophysiology of motor dysfunction in Parkinson's disease as the rationale for drug treatment and rehabilitation. *Parkinsons Dis.* **2016**, 9832839 (2016).
6. Ferrazzoli, D. et al. Basal ganglia and beyond: the interplay between motor and cognitive aspects in Parkinson's disease rehabilitation. *Neurosci. Biobehav. Rev.* **90**, 294–308 (2018).
7. Nowak, M., Zich, C. & Stagg, C. J. Motor cortical gamma oscillations: what have we learnt and where are we headed?. *Curr. Behav. Neurosci. Rep.* **5**, 136–142 (2018).
8. Guerra, A. et al. Enhancing gamma oscillations restores primary motor cortex plasticity in Parkinson's disease. *J. Neurosci.* **40**, 4788–4796 (2020).
9. Chu, H.-Y. et al. Dysfunction of motor cortices in Parkinson's disease. *Cereb. Cortex* **34**, 1–24 (2024).
10. Buzsáki, G. & Wang, X.-J. Mechanisms of gamma oscillations. *Annu. Rev. Neurosci.* **35**, 203–225 (2012).
11. Hijazi, S., Smit, A. B. & van Kesteren, R. E. Fast-spiking parvalbumin-positive interneurons in brain physiology and Alzheimer's disease. *Mol. Psychiatry* **28**, 4954–4967 (2023).
12. Rupert, D. D. & Shea, S. D. Parvalbumin-positive interneurons regulate cortical sensory plasticity in adulthood and development through shared mechanisms. *Front. Neural Circuits* **16**, 886629 (2022).
13. Milicevic, K. D. et al. Physiological features of parvalbumin-expressing GABAergic interneurons contributing to high-frequency oscillations in the cerebral cortex. *Curr. Res. Neurobiol.* **6**, 100121 (2024).
14. He, Q. et al. Early synaptic dysfunction of striatal parvalbumin interneurons in a mouse model of Parkinson's disease. *iScience* **27**, 111253 (2024).
15. Swanson, O. K. & Maffei, A. From hiring to firing: activation of inhibitory neurons and their recruitment in behavior. *Front. Mol. Neurosci.* **12**, 168 (2019).
16. Swanson, O. K., Yevoo, P. E., Richard, D. & Maffei, A. Altered thalamocortical signaling in a mouse model of Parkinson's disease. *J. Neurosci.* **43**, 6021–6034 (2023).
17. Masini, D. et al. A guide to the generation of a 6-hydroxydopamine mouse model of Parkinson's disease for the study of non-motor symptoms. *Biomedicines* **9**, 1–19 (2021).
18. Donoghue, T. et al. Parameterizing neural power spectra into periodic and aperiodic components. *Nat. Neurosci.* **23**, 1655–1665 (2020).
19. Spalletti, C. et al. A robotic system for quantitative assessment and poststroke training of forelimb retraction in mice. *Neurorehabil. Neural Repair* **28**, 188–196 (2014).
20. Pasquini, M. et al. A robotic system for adaptive training and function assessment of forelimb retraction in mice. *IEEE Trans. Neural Syst. Rehabil. Eng.* **26**, 1803–1812 (2018).
21. Spalletti, C. et al. Combining robotic training and inactivation of the healthy hemisphere restores pre-stroke motor patterns in mice. *Elife* **6**, 1–31 (2017).
22. Hadler, M. D., Tzilivaki, A., Schmitz, D., Alle, H. & Geiger, J. R. P. Gamma oscillation plasticity is mediated via parvalbumin interneurons. *Sci. Adv.* **10**, eadj7427 (2024).
23. Kriener, B., Hu, H. & Vervaeke, K. Parvalbumin interneuron dendrites enhance gamma oscillations. *Cell Rep.* **39**, 110948 (2022).
24. Cho, K. K. A. et al. Cross-hemispheric gamma synchrony between prefrontal parvalbumin interneurons supports behavioral adaptation during rule shift learning. *Nat. Neurosci.* **23**, 892–902 (2020).
25. Chen, L., Daniels, S., Dvorak, R. & Chu, H.-Y. Reduced thalamic excitation to motor cortical pyramidal tract neurons in parkinsonism. *Sci. Adv.* **9**, eadg3038 (2023).
26. Villalba, R. M., Behnke, J. A., Pare, J.-F. & Smith, Y. Comparative ultrastructural analysis of thalamocortical innervation of the primary motor cortex and supplementary motor area in control and MPTP-treated parkinsonian monkeys. *Cereb. Cortex* **31**, 3408–3425 (2021).
27. Hong, S. & Stevens, B. Microglia: phagocytosing to clear, sculpt, and eliminate. *Dev. Cell* **38**, 126–128 (2016).
28. Isik, S., Yeman Kiyak, B., Akbayir, R., Seyhali, R. & Arpaci, T. Microglia mediated neuroinflammation in Parkinson's disease. *Cells* **12**, 1012 (2023).
29. Zhang, W., Xiao, D., Mao, Q. & Xia, H. Role of neuroinflammation in neurodegeneration development. *Signal Transduct. Target. Ther.* **8**, 267 (2023).
30. Cangalaya, C. et al. Real-time mechanisms of exacerbated synaptic remodeling by microglia in acute models of systemic inflammation and tauopathy. *Brain Behav. Immun.* **110**, 245–259 (2023).
31. Salter, M. W. & Stevens, B. Microglia emerge as central players in brain disease. *Nat. Med.* **23**, 1018–1027 (2017).
32. Krukowski, K. et al. Novel microglia-mediated mechanisms underlying synaptic loss and cognitive impairment after traumatic brain injury. *Brain Behav. Immun.* **98**, 122–135 (2021).
33. Holness, C. L. & Simmons, D. L. Molecular cloning of CD68, a human macrophage marker related to lysosomal glycoproteins. *Blood* **81**, 1607–1613 (1993).
34. Simola, N., Morelli, M. & Carta, A. R. The 6-hydroxydopamine model of Parkinson's disease. *Neurotox. Res.* **11**, 151–167 (2007).
35. Whalen, T. C., Willard, A. M., Rubin, J. E. & Gittis, A. H. Delta oscillations are a robust biomarker of dopamine depletion severity and motor dysfunction in awake mice. *J. Neurophysiol.* **124**, 312–329 (2020).
36. Chen, H., Lei, H. & Xu, Q. Neuronal activity pattern defects in the striatum in awake mouse model of Parkinson's disease. *Behav. Brain Res.* **341**, 135–145 (2018).
37. Ohara, S. et al. Increased synchronization of cortical oscillatory activities between human supplementary motor and primary sensorimotor areas during voluntary movements. *J. Neurosci.* **21**, 9377–9386 (2001).
38. Fries, P. A mechanism for cognitive dynamics: neuronal communication through neuronal coherence. *Trends Cogn. Sci.* **9**, 474–480 (2005).
39. Fries, P. Rhythms for cognition: communication through coherence. *Neuron* **88**, 220–235 (2015).
40. Ortega, A. et al. Cortical beta oscillation in brain slices of hemi Parkinsonian mice. *Neurosci. Lett.* **849**, 138128 (2025).
41. Medeiros, D., de, C. et al. A mouse model of sleep disorders in Parkinson's disease showing distinct effects of dopamine D2-like receptor activation. *Prog. Neurobiol.* **231**, 102536 (2023).
42. Pollok, B., Latz, D., Krause, V., Butz, M. & Schnitzler, A. Changes of motor-cortical oscillations associated with motor learning. *Neuroscience* **275**, 47–53 (2014).
43. Wright, D. J., Holmes, P., Di Russo, F., Loporto, M. & Smith, D. Reduced motor cortex activity during movement preparation following a period of motor skill practice. *PLoS ONE* **7**, e51886 (2012).
44. Barrese, J. C. et al. Failure mode analysis of silicon-based intracortical microelectrode arrays in non-human primates. *J. Neural Eng.* **10**, 066014 (2013).
45. Grissom, N. & Bhatnagar, S. Habituation to repeated stress: get used to it. *Neurobiol. Learn. Mem.* **92**, 215–224 (2009).
46. Mazzoni, A., Panzeri, S., Logothetis, N. K. & Brunel, N. Encoding of naturalistic stimuli by local field potential spectra in networks of excitatory and inhibitory neurons. *PLoS Comput. Biol.* **4**, e1000239 (2008).

47. Meneghetti, N. et al. Narrow and broad γ bands process complementary visual information in mouse primary visual cortex. *eNeuro* **8**, ENEURO.0106–21.2021 (2021).
48. Meneghetti, N. et al. Synaptic alterations in visual cortex reshape contrast-dependent gamma oscillations and inhibition-excitation ratio in a genetic mouse model of migraine. *J. Headache Pain***23**, 125 (2022).
49. Brunel, N. & Wang, X.-J. What determines the frequency of fast network oscillations with irregular neural discharges? I. Synaptic dynamics and excitation-inhibition balance. *J. Neurophysiol.* **90**, 415–430 (2003).
50. Ray, S. & Maunsell, J. H. R. Different origins of gamma rhythm and high-gamma activity in macaque visual cortex. *PLoS Biol.* **9**, e1000610 (2011).
51. Buzsáki, G. & da Silva, F. L. High frequency oscillations in the intact brain. *Prog. Neurobiol.* **98**, 241–249 (2012).
52. Meneghetti, N., Vannini, E. & Mazzoni, A. Rodents' visual gamma as a biomarker of pathological neural conditions. *J. Physiol.* **602**, 1017–1048 (2024).
53. Sohal, V. S., Zhang, F., Yizhar, O. & Deisseroth, K. Parvalbumin neurons and gamma rhythms enhance cortical circuit performance. *Nature* **459**, 698–702 (2009).
54. Izaki, Y. & Akema, T. Gamma-band power elevation of prefrontal local field potential after posterior dorsal hippocampus-prefrontal long-term potentiation induction in anesthetized rats. *Exp. Brain Res.* **184**, 249–253 (2008).
55. Vignozzi, L. et al. Combining Gamma neuromodulation and robotic rehabilitation restores parvalbimin-mediated Gamma function and boosts motor recovery in stroke mice. *bioRxiv* https://doi.org/10.1101/2024.08.15.608060 (2024).
56. Steiner, H. & Kitai, S. T. Unilateral striatal dopamine depletion: time-dependent effects on cortical function and behavioural correlates. *Eur. J. Neurosci.* **14**, 1390–1404 (2001).
57. Linen, S. R., Chang, N. H., Hess, E. J., Stanley, G. B. & Waiblinger, C. Sensory-behavioral deficits in Parkinson's disease: insights from a 6-OHDA mouse model. *bioRxivorg* https://doi.org/10.1101/2024.06.05.597339 (2024).
58. Rocchi, F. et al. Increased fMRI connectivity upon chemogenetic inhibition of the mouse prefrontal cortex. *Nat. Commun.* **13**, 1056 (2022).
59. Brunetti, E., Maldonado, P. E. & Aboitiz, F. Phase synchronization of delta and theta oscillations increase during the detection of relevant lexical information. *Front. Psychol.* **4**, 308 (2013).
60. Brier, L. M. et al. Separability of calcium slow waves and functional connectivity during wake, sleep, and anesthesia. *Neurophotonics* **6**, 035002 (2019).
61. Bavelier, D., Levi, D. M., Li, R. W., Dan, Y. & Hensch, T. K. Removing brakes on adult brain plasticity: from molecular to behavioral interventions. *J. Neurosci.* **30**, 14964–14971 (2010).
62. Zeiler, S. R. et al. Medial premotor cortex shows a reduction in inhibitory markers and mediates recovery in a mouse model of focal stroke. *Stroke* **44**, 483–489 (2013).
63. Ng, K. L. et al. Fluoxetine maintains a state of heightened responsiveness to motor training early after stroke in a mouse model. *Stroke* **46**, 2951–2960 (2015).
64. Shepherd, G. M. G. Corticostriatal connectivity and its role in disease. *Nat. Rev. Neurosci.* **14**, 278–291 (2013).
65. Cherian, S., Simms, G., Chen, L. & Chu, H.-Y. Loss of midbrain dopamine neurons does not alter GABAergic inhibition mediated by parvalbumin-expressing interneurons in mouse primary motor cortex. *eNeuro* **11**, ENEURO.0010–24.2024 (2024).
66. Ruden, J. B., Dugan, L. L. & Konradi, C. Parvalbumin interneuron vulnerability and brain disorders. *Neuropsychopharmacology* **46**, 279–287 (2021).
67. Smeralda, C. L. et al. The role of parvalbumin interneuron dysfunction across neurodegenerative dementias. *Ageing Res. Rev.* **101**, 102509 (2024).
68. Lu, J.-S. et al. Cellular and synaptic mechanisms for Parkinson's disease-related chronic pain. *Mol. Pain***17**, 1744806921999025 (2021).
69. Mallet, N., Delgado, L., Chazalon, M., Miguelez, C. & Baufreton, J. Cellular and synaptic dysfunctions in Parkinson's disease: stepping out of the striatum. *Cells* **8**, 1–29 (2019).
70. Bjorklund, A. Dopamine-containing systems in the CNS. in *Handbook of Chemical Neuroanatomy: Classical Transmitters in the CNS,* Vol. 2, *Elsevier* 55–122 (1984).
71. Björklund, A. & Dunnett, S. B. Dopamine neuron systems in the brain: an update. *Trends Neurosci.* **30**, 194–202 (2007).
72. Luo, P. et al. Whole brain mapping of long-range direct input to glutamatergic and GABAergic neurons in motor cortex. *Front. Neuroanat.* **13**, 44 (2019).
73. Gardoni, F. & Bellone, C. Modulation of the glutamatergic transmission by Dopamine: a focus on Parkinson, Huntington and Addiction diseases. *Front. Cell. Neurosci.* **9**, 25 (2015).
74. Jeong, M. et al. Comparative three-dimensional connectome map of motor cortical projections in the mouse brain. *Sci. Rep.* **6**, 20072 (2016).
75. Çınar, E., Tel, B. C. & Şahin, G. Neuroinflammation in Parkinson's disease and its treatment opportunities. *Balk. Med. J.* **39**, 318–333 (2022).
76. Wang, Q., Liu, Y. & Zhou, J. Neuroinflammation in Parkinson's disease and its potential as therapeutic target. *Transl. Neurodegener.* **4**, 19 (2015).
77. McGeer, P. L. & McGeer, E. G. Inflammation and neurodegeneration in Parkinson's disease. *Parkinsonism Relat. Disord.* **10**, S3–7 (2004).
78. Mattioli, F., Maglianella, V., D'Antonio, S., Trimarco, E. & Caligiore, D. Non-invasive brain stimulation for patients and healthy subjects: current challenges and future perspectives. *J. Neurol. Sci.* **456**, 122825 (2024).
79. Tiberi, A. et al. Reversal of neurological deficits by painless nerve growth factor in a mouse model of Rett syndrome. *Brain* **147**, 122–134 (2024).
80. Stoffers, D. et al. Increased cortico-cortical functional connectivity in early-stage Parkinson's disease: an MEG study. *Neuroimage* **41**, 212–222 (2008).
81. Silberstein, P. et al. Cortico-cortical coupling in Parkinson's disease and its modulation by therapy. *Brain* **128**, 1277–1291 (2005).
82. Lundblad, M., Picconi, B., Lindgren, H. & Cenci, M. A. A model of L-DOPA-induced dyskinesia in 6-hydroxydopamine lesioned mice: relation to motor and cellular parameters of nigrostriatal function. *Neurobiol. Dis.* **16**, 110–123 (2004).
83. Grealish, S., Mattsson, B., Draxler, P. & Björklund, A. Characterisation of behavioural and neurodegenerative changes induced by intranigral 6-hydroxydopamine lesions in a mouse model of Parkinson's disease. *Eur. J. Neurosci.* **31**, 2266–2278 (2010).
84. Lai, S. et al. Quantitative kinematic characterization of reaching impairments in mice after a stroke. *Neurorehabil. Neural Repair* **29**, 382–392 (2015).
85. Anjum, M. F. et al. Linear predictive approaches separate field potentials in animal model of Parkinson's disease. *Front. Neurosci.* **14**, 1–15 (2020).
86. Wu, Y., Lu, L., Qing, T., Shi, S. & Fang, G. Transient increases in neural oscillations and motor deficits in a mouse model of Parkinson's disease. *Int. J. Mol. Sci.* **25**, 9545 (2024).
87. Minetti, A. Unlocking the potential of adeno-associated virus in neuroscience: a brief review. *Mol. Biol. Rep.* **51**, 563 (2024).
88. Montagni, E. et al. Mapping brain state-dependent sensory responses across the mouse cortex. *iScience* **27**, 109692 (2024).

89. Conti, E., Allegra Mascaro, A. L. & Pavone, F. S. Large scale double-path illumination system with split field of view for the all-optical study of inter-and intra-hemispheric functional connectivity on mice. *Methods Protoc.* **2**, 1–11 (2019).
90. Zalesky, A., Fornito, A. & Bullmore, E. T. Network-based statistic: identifying differences in brain networks. *Neuroimage* **53**, 1197–1207 (2010).
91. Nakai, N. et al. Virtual reality-based real-time imaging reveals abnormal cortical dynamics during behavioral transitions in a mouse model of autism. *Cell Rep.* **42**, 112258 (2023).
92. Schallert, T. et al. Motor rehabilitation, use-related neural events, and reorganization of the brain after injury. in *Cerebral Reorganization of Function After Brain Damage* 145–167 (New York, NY, 2000; online edn, Oxford Accademy, 2000).
93. Bonito-Oliva, A. et al. Cognitive impairment and dentate gyrus synaptic dysfunction in experimental parkinsonism. *Biol. Psychiatry* **75**, 701–710 (2014).
94. Heeringa, A. N. et al. Glutamatergic projections to the cochlear nucleus are redistributed in tinnitus. *Neuroscience* **391**, 91–103 (2018).
95. Conti, S. et al. Combining robotics with enhanced serotonin-driven cortical plasticity improves post-stroke motor recovery. *Prog. Neurobiol.* **203**, 102073 (2021).
96. Ippolito, D. M. & Eroglu, C. Quantifying synapses: an immunocytochemistry-based assay to quantify synapse number. *J. Vis. Exp*. https://doi.org/10.3791/2270 (2010).
97. Baroncelli, L. et al. A mouse model for creatine transporter deficiency reveals early onset cognitive impairment and neuropathology associated with brain aging. *Hum. Mol. Genet.* **25**, 4186–4200 (2016).
98. Alia, C. et al. Reducing GABAA-mediated inhibition improves forelimb motor function after focal cortical stroke in mice. *Sci. Rep.* **6**, 37823 (2016).
99. Tiberi, A. *AlexiaTiberi/MicroNeuSeg: A Python-Based Software for the Spatial Distribution Analysis of Microglia and Neurons* (Zenodo, 2025).
100. Totaro, V., Lupori, L. & Pizzorusso, T. *CounTastic: A MATLAB-Based Software for Cell Counting* (Zenodo, 2025).
101. Schafer, D. P., Lehrman, E. K., Heller, C. T. & Stevens, B. An engulfment assay: a protocol to assess interactions between CNS phagocytes and neurons. *J. Vis. Exp.* https://doi.org/10.3791/51482 (2014).

Acknowledgements

The study was funded by Fondo Beneficenza Intesa San Paolo n. B/2022/0193, Project "ONDA", Project Manager: Cristina Spalletti, and from THE Tuscany Health Ecosystem ECS_00000017 MUR_ PNRR, Project Manager: Anna Letizia Allegra Mascaro. We thank Francesca Biondi (CNR Pisa) for the excellent animal care, Maria Pasquini, Elena Novelli and Renzo di Renzo for technical support with imaging and informatics. Figures drowing were made by the use of BioRender upon license (https://BioRender.com/senecaj).

Author contributions

Conceptualization: C.S., A.L.A.M. A.Maz., and S.C.; methodology: C.S., A.L.A.M., A.Maz., and S.C.; investigation: A.Mi., F.M., A.Mar., E.M., E.C., A.T., N.M., A.Maz., A.L.A.M., C.S., and S.C.; writing—original draft: A.Mi., E.M., N.M., A.Maz., A.L.A.M., S.C., and C.S., writing—review & editing: A.Mi., E.M., E.C., A.T., N.M., A.Maz., A.L.A.M., S.C., and C.S; funding acquisition: C.S., A.L.A.M., and A.Maz.; resources: C.S., A.L.A.M., and A.Maz., supervision: C.S., A.L.A.M., A.Maz., and S.C.

Competing interests

The authors declare no competing interests.

Additional information

Supplementary information The online version contains supplementary material available at https://doi.org/10.1038/s41531-025-01052-6.

Correspondence and requests for materials should be addressed to Cristina Spalletti.